# Microtubule stiffening by the doublecortin-domain protein ZYG-8 contributes to mitotic spindle orientation during zygote division in Caenorhabditis elegans.

Louis Cueff, Ewen Huet, Loïc Schmitt, Sylvain Pastezeur, Méline Coquil, Talia Savary, Jacques Pécréaux, Hélène Bouvrais

**Microtubule stiffening by the doublecortin-domain protein ZYG-8 contributes to mitotic spindle orientation during zygote division in *Caenorhabditis elegans.***

Louis Cueff[1], Ewen Huet[1], Loïc Schmitt[1], Sylvain Pastezeur[1], Méline Coquil[1], Talia Savary[1], Jacques Pécréaux[1,*], Hélène Bouvrais[1,*]

Affiliations:
[1] CNRS, Univ Rennes, IGDR (Institut de Génétique et Développement de Rennes) – UMR 6290, F-35000 Rennes, France
* Corresponding authors :
Jacques Pécréaux (ORCID : 0000-0001-9998-4844) and Hélène Bouvrais (ORCID : 0000-0003-1128-1322)
IGDR-UMR6290, CNRS-Université de Rennes
Faculté de Médecine
2 Av. du Professeur Léon Bernard,
CS 34317 - 35043 Rennes Cedex
France
Tel: +33 2 23 23 45 03 (JP), +33 2 23 23 40 08 (HB)
Email: jacques.pecreaux@univ-rennes.fr, helene.bouvrais@univ-rennes.fr

**ABSTRACT**

In *Caenorhabditis elegans*, mutations in *zyg-8*$^{DCLK1}$, the sole Doublecortin-family member, led to incorrect mitotic spindle positioning, as seen by immunofluorescence. Doublecortin proteins bind to microtubules and are thought to stabilise or rigidify microtubules. Upon targeting *zyg-8*, we observed altered spindle-pole oscillations and perturbations in microtubule cortical-contact behaviour. They were not accounted for solely by the previously reported changes in microtubule dynamics. Instead, the phenotypes were consistent with ZYG-8 increasing microtubule rigidity. ZYG-8 depletion or mutation led to more frequent microtubule bending, and higher curvature and tortuosity. Microtubule softening in *zyg-8* mutants likely reduced the efficiency of centring forces, causing exaggerated spindle oscillations and subsequent mispositioning during late anaphase. We propose that sufficient microtubule rigidity is essential for generating effective cortical pushing forces, which act as centring mechanisms to ensure accurate spindle orientation in late mitosis. These findings may have implications for cancer therapy, since the expression of DCLK1 and Tau, both known regulators of microtubule rigidity, is often deregulated in human cancers.

## INTRODUCTION

Microtubules are semi-rigid polymers that form a crucial component of the cell cytoskeleton alongside actin and intermediate filaments. In coordination with molecular motors and microtubule-associated proteins (MAPs), microtubules perform essential functions, including cell shaping [1, 2], intracellular trafficking [3], and cell migration [4]. Microtubules also play major roles in cell division; for example, spindle microtubules assemble into the mitotic spindle and segregate chromosomes, while astral microtubules help position the spindle [5-11]. Along a structural line, each microtubule comprises protofilaments that are linear chains of tubulin dimers added or removed dynamically. Microtubule dynamic instability, characterised by stochastic transitions between growing and shrinking phases, is regulated *in vivo* by numerous MAPs [12-14]. The mechanical properties of microtubules, particularly their flexural rigidity—i.e., their resistance to bending—have received comparatively less attention. Notably, microtubules exhibit the highest flexural rigidity among cytoskeletal filaments [15]. While *in vitro* reconstituted microtubules are bent at the scale of a few millimetres [15-18], *in vivo* observations revealed that microtubules appear bent at the micrometre scale [19-21]. On one hand, high microtubule rigidity is necessary for efficient intracellular trafficking [22], for generating pushing forces against the cell periphery that contribute to spindle or nucleus positioning [23-28], or for exerting pushing forces on chromosome arms to produce the polar ejection force with the assistance of chromokinesins [29, 30]. On the other hand, microtubules must also be flexible enough to bend, for example when growing through the crowded cytoplasm [31]. This highlights the need to regulate microtubule flexural rigidity *in vivo* to support its various biological functions [21].

Research, particularly in neuronal systems, has identified two major protein families involved in regulating microtubule rigidity. These are the Doublecortin family, which includes DCX and DCLK1, and the MAP2/MAP4/Tau superfamily [16, 18, 32, 33]. For instance, the simultaneous knockdown of DCX and DCLK1 in rat neurons led to more curved microtubules at the growing axon tip [34]. Doublecortin-family proteins associate with microtubules through their doublecortin domains. Notably, these proteins bind between the microtubule protofilaments at the vertices of four tubulin dimers, contributing to the lateral coupling of adjacent protofilaments [35, 36]. This binding likely restricts protofilament sliding, thereby increasing microtubule rigidity [37, 38]. Along a similar line, Tau-deficient axons have been shown to exhibit curled microtubules [39]. Tau family proteins bind longitudinally along the outer ridges of microtubule protofilaments. It would strengthen the longitudinal contacts between tubulin heterodimers within a protofilament, straightening the protofilaments [32, 40, 41]. Importantly, both protein families could also contribute to the regulation of microtubule dynamics, making it challenging to disentangle their roles in mechanical versus dynamic regulation. Some *in vivo* studies indicate that these proteins stabilise microtubules and/or promotes their growth [39, 42]. They may reduce their dynamics by decreasing catastrophe frequency, depolymerisation and nucleation rates [42-44]. While the impacts of controlling microtubule rigidity have primarily been studied in neurons, microtubule-rigidity contribution during cell division also warrants investigations.

Previous studies on cell division involving the targeting of proteins from the Doublecortin and Tau families revealed several defects. These included mitotic spindle mispositioning, abnormalities in spindle formation and integrity, and impaired cell cycle progression [45-51]. During neurogenesis, altered expression of Doublecortin-family proteins led to incorrect cell

fate determination for neural progenitors [45, 46]. Additionally, the deregulation of Tau (whether through mutation or overexpression) resulted in mitotic defects, such as issues with spindle formation, aneuploidy and chromosome misalignment [52, 53]. Thus, targeting Doublecortin or Tau family proteins can lead to a wide range of meiotic and mitotic disturbances, although the underlying mechanisms remain unclear. Proposed explanations include perturbations in microtubule stability, and in molecular motor activity or recruitment [45-50, 54]. Whether the underlying mechanism could involve microtubule rigidity is yet to be investigated.

In the *Caenorhabditis elegans* zygote, the pronuclei-centrosome complex (NCC) and the mitotic spindle exhibit stereotyped movements during cell division [55]. It makes this system a well-established model for studying asymmetric divisions. In these divisions, the correct positioning and orientation of the spindle are critical for cell fate determination and, more broadly, for the organism's development [9]. In further detail, the NCC forms at the zygote posterior pole, migrates anteriorly, and the centrosomes align with the anteroposterior axis during prophase. The mitotic spindle assembles near the cell centre after the nuclear envelop breakdown (NEBD), remains centred during metaphase, and is then positioned posteriorly, mainly during anaphase [56]. During this posterior displacement, the spindle undergoes transverse oscillations driven by strong cortical pulling forces [57]. While not essential for asymmetric division, these oscillations have been instrumental in studying spindle positioning forces [58-63]. Astral microtubules, which emanate from the centrosomes, play a central role in spindle movements. These microtubules can transmit or generate three types of forces [5, 7, 64]: first, cortical pulling forces mediated by dynein motors anchored at the cell cortex interacting with shrinking microtubules [58, 65, 66]; second, cytoplasmic pulling forces that are reaction forces generated by organelle movement along microtubules, driven by dynein motors [67]; and third, cortical pushing forces generated by microtubules that grow against the cell cortex [25, 27, 68]. Various models have addressed the roles of these forces. Kimura *et al.* proposed that cytoplasmic pulling forces contribute to NCC centration [67], while others have suggested that these forces do not aid in maintaining spindle position at the cell centre during metaphase [25] or in driving anaphase spindle oscillations [59]. Cortical pulling forces, which are stronger at the posterior, are well-established drivers of posterior spindle displacement and anaphase oscillations [58-60, 66, 69, 70]. However, a restoring force must exist during spindle-pole oscillations, notably to stabilise the spindle position against these strong cortical pulling forces and permit oscillations. This centring mechanism could arise from the embryo's geometry [59, 66] or microtubule dynamics [58]. Alternative mechanisms include cytoplasmic pulling forces or cortical pushing forces. The latter may result from astral microtubules pushing against the cortex or from microtubule buckling [27, 57, 58]. We and others suggested that microtubule buckling—bending under compressive load—contributes to centring the spindle, in particular for spindle maintenance at the cell centre during metaphase [25, 27, 68, 71]. It positions the flexural rigidity of microtubules as a candidate key factor in spindle choreography. We envisioned that sufficiently high microtubule rigidity is necessary to enable stronger cortical pushing forces. These forces may be required to counterbalance elevated cortical pulling forces during anaphase.

In *C. elegans* zygote, mutations in *zyg-8*$^{dclk1}$, the sole Doublecortin family member, have been shown to cause improper spindle positioning during anaphase, as observed through immunofluorescence and DIC microscopy [48, 72]. ZYG-8 contains a kinase domain at the C-terminus and two doublecortin (DC) domains at the N-terminus, the latter enabling its binding

to microtubules. Studies of the human homolog DCLK1 revealed that its kinase domain auto-phosphorylates the DC domains. Besides, hyperphosphorylation of these domains reduces DCLK1's binding affinity to microtubules [73]. In *C. elegans* zygote, mutations in either domain of *zyg-8* led to spindle orientation defects [48]. It has been proposed that ZYG-8 promotes microtubule assembly, which is required for correct spindle positioning [48, 72]. Interestingly, Srayko *et al.* found that ZYG-8 contributes to microtubule growth, although to a lesser extent compared to the well-established polymerase ZYG-9$^{XMAP215}$ [42]. Besides, ZYG-8 was shown to limit astral microtubule nucleation, although the perturbations were less pronounced than those observed with *spd-2$^{CEP192}$(RNAi)* [42]. Could these moderate effects on microtubule dynamics cause by depleting ZYG-8 be sufficient to explain the spindle mis-positioning seen in *zyg-8* mutants during anaphase? To address this question and better understand ZYG-8's role in spindle positioning, we used modern microscopy techniques that allow dynamic studies in live embryos, along with advanced image analysis. We explored the potential roles of ZYG-8 in regulating both microtubule dynamics and flexural rigidity. We applied three complementary genetic perturbations: RNAi-mediated depletion of ZYG-8, overexpression, and the thermosensitive *zyg-8(or484ts)* mutant that disrupts microtubule binding [72]. Upon targeting *zyg-8*, we analysed anaphase spindle oscillations and microtubule cortical contacts. We found that the observed changes could not be explained solely by altered microtubule dynamics. This prompted us to investigate whether ZYG-8 also regulates microtubule rigidity during zygote division. To assess changes in microtubule rigidity, we measured the distributions of microtubule local curvatures. We also examined spindle positioning forces using two biophysical assays. Our results demonstrated that ZYG-8 is needed to maintain the correct spindle orientation during mitosis, primarily by permitting high centring forces that depend on the microtubule flexural rigidity. Interestingly, RNAi depletion of PTL-1, the sole member of the Tau/MAPT family, produced a similar but milder effect on spindle choreography. Overall, our study highlights the need for sufficient microtubule rigidity for proper mitotic spindle positioning and orientation during *C. elegans* zygote division.

## RESULTS

### 1- ZYG-8 affects spindle-pole oscillations beyond microtubule growth and nucleation.

In *C. elegans* zygotes, mutations in *zyg-8$^{dclk1}$* disrupted spindle positioning, particularly during anaphase, as shown by DIC microscopy recordings [48, 72]. These mutations were proposed to perturb astral microtubule stability, as microtubules stained with anti-tubulin antibodies appeared shorter. Immunofluorescence revealed that ZYG-8 localises at least to the spindle and its poles [48]. To investigate its association with astral microtubules, we generated three strains using CRISPR-Cas9 genome editing: one expressing fluorescently tagged ZYG-8 (mNeonGreen::ZYG-8) from the endogenous locus; a second with *zyg-8* tagged at the locus with three OLLAS epitope tags; and a third carrying an integrated transgene overexpressing *zyg-8* (*pPie-1*::mNG::3*OLLAS::ZYG-8) in addition to the endogenous copy (Table S1). During the first embryonic division, in both endogenously expressed and overexpressed *zyg-8* strains, ZYG-8 showed significant co-localisation with astral and spindle microtubules (Figure S1, Method M5). This localisation was consistent with its previously proposed role in promoting microtubule assembly [48].

Previous studies in *C. elegans* zygotes focussing on ZYG-8 have either examined its role in spindle positioning using *zyg-8* mutants or investigated its effects on microtubule dynamics

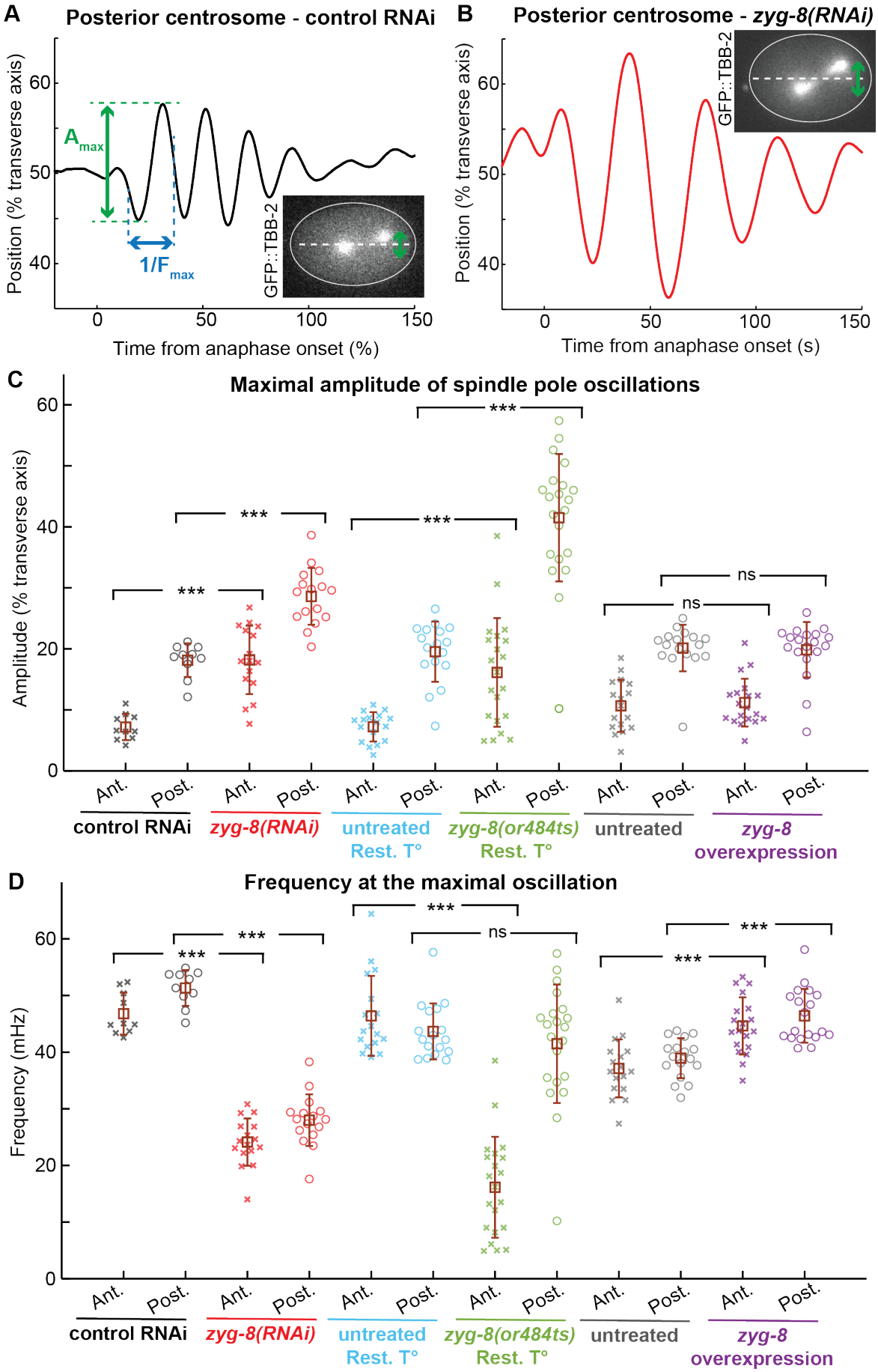
A
Posterior centrosome - control RNAi
Position (% transverse axis)
60
50
40
A max
1/F max
GFP::TBB-2
0
50
100
150
Time from anaphase onset (%)
B
Posterior centrosome - zyg-8(RNAi)
Position (% transverse axis)
GFP::TBB-2
Time from anaphase onset (s)
C
Maximal amplitude of spindle pole oscillations
Amplitude (% transverse axis)
***
ns
Ant.
Post.
control RNAi
zyg-8(RNAi)
untreated
Rest. T°
zyg-8(or484ts)
Rest. T°
untreated
zyg-8
overexpression
D
Frequency at the maximal oscillation
Frequency (mHz)

**Figure 1: ZYG-8 limits spindle-pole oscillation amplitudes and increases their frequencies during anaphase.**
(**A-B**) Exemplar posterior centrosome positions along the transverse axis for (A) a control RNAi embryo and (B) a *zyg-8(RNAi)*-treated embryo. Maximal amplitude is highlighted in green, while its frequency is annotated in blue. We applied a moving-average filter over a window size of 5 s to smooth the centrosome positions. Exemplar images used for centrosome analysis with a GFP::TBB-2 fluorescent labelling. (**C**) Maximal oscillation amplitudes and (**D**) their frequencies for the (cross) anterior and (circle) posterior centrosomes during anaphase. We tracked the centrosomes and analysed their positions in: (red) *N* = 16 *zyg-8(RNAi)*-treated embryos and (black) *N* = 10 control RNAi embryos expressing GFP::TBB-2; (light green) *N* = 21 *zyg-8(or484ts)* mutants and (light blue) *N* = 17 untreated embryos, both at the restrictive temperature (Rest. T°) expressing GFP::TBB-2; (purple) *N* = 19 *zyg-8* overexpressing embryos and (grey) *N* = 17 untreated embryos expressing mCherry::tubulin (Method M7). The brown squares and error bars correspond to the means and SD. *** indicates significant differences ($p \leq 1x10^{-4}$) and ns denotes non-significant differences ($p > 0.05$) (Method M14). Exemplar posterior centrosome positions along the transverse axis, along with representative images for a *zyg-8(or484ts)* mutant and an untreated embryo, both at the restrictive temperature, are shown in Figure S3.

through *zyg-8(RNAi)* treatment [42, 48, 72]. We sought to complement these studies by introducing three distinct genetic perturbations targeting *zyg-8*. First, we used the thermosensitive mutant *zyg-8(or484ts)*, which carries a mutation in the first doublecortin domain [48, 74]. This mutant has been reported to prevent ZYG-8's ability to bind microtubules when maintained at the restrictive temperature of 25°C for more than 12 hours [72]. Second, we used the strain described above that overexpresses ZYG-8. Western blot analysis of worm lysates revealed increased OLLAS levels, indicated elevated ZYG-8 expression, as the OLLAS tag was inserted into the overexpression transgene (Figure S2A, Method M6). Besides, mNG::ZYG-8 fluorescence on both spindle and astral microtubules in zygotes increased approximately threefold (Figure S2C, D & G, Method M6). Third, we reduced ZYG-8 expression using RNAi. Western blot analysis of worm lysates from the strain carrying OLLAS-tagged *zyg-8* showed decreased OLLAS levels upon *zyg-8(RNAi)*, indicating reduced ZYG-8 expression (Figure S2B, Method M6). Besides, we observed an approximately fivefold decrease in mNG::ZYG-8 fluorescence on zygotic microtubules upon *zyg-8(RNAi)* (Figure S2E, F & H, Method M6). These genetic perturbations—loss of ZYG-8 from microtubules, overexpression, and partial depletion—provided the tools to investigate how different ZYG-8 levels affect mitotic spindle choreography.

Since ZYG-8 has been proposed to play a key role in spindle positioning, particularly during anaphase, we focussed on spindle pole oscillations occurring at this stage [57]. These oscillations have been widely used in previous studies to assess perturbations in spindle-positioning forces [58-60, 62, 63]. We quantified both the amplitude and frequency of the maximal oscillation at each spindle pole in strains expressing GFP::TBB-2 (*zyg-8(RNAi)* or *zyg-8* mutants) or mCherry::tubulin (*zyg-8* overexpression) (Method M7). Following *zyg-8(RNAi)*, we observed a large increase in oscillation amplitudes (Figure 1A-C) and a major decrease in frequencies (Figure 1A, B & D). In *zyg-8(or484ts)* mutants at the restrictive temperature, oscillation amplitudes were further elevated (Figures 1C and S3). In mutants, oscillation frequencies at the anterior centrosome were further decreased compared to RNAi treatment, while those at the posterior centrosome were more variable than in other conditions – likely due to spindle misorientation – and therefore not significantly affected (Figure 1D). The stronger phenotype in mutant embryos compared to *zyg-8(RNAi)*-treated embryos was

consistent with the partial depletion of ZYG-8 by RNAi (Figure S2B, H). These results suggested that ZYG-8 acts to limit spindle oscillation amplitudes during anaphase. In embryos overexpressing *zyg-8*, maximal amplitudes remained unchanged (Figure 1C), but oscillation frequencies increased significantly (Figure 1D), indicating that oscillation frequency depends on ZYG-8 levels.

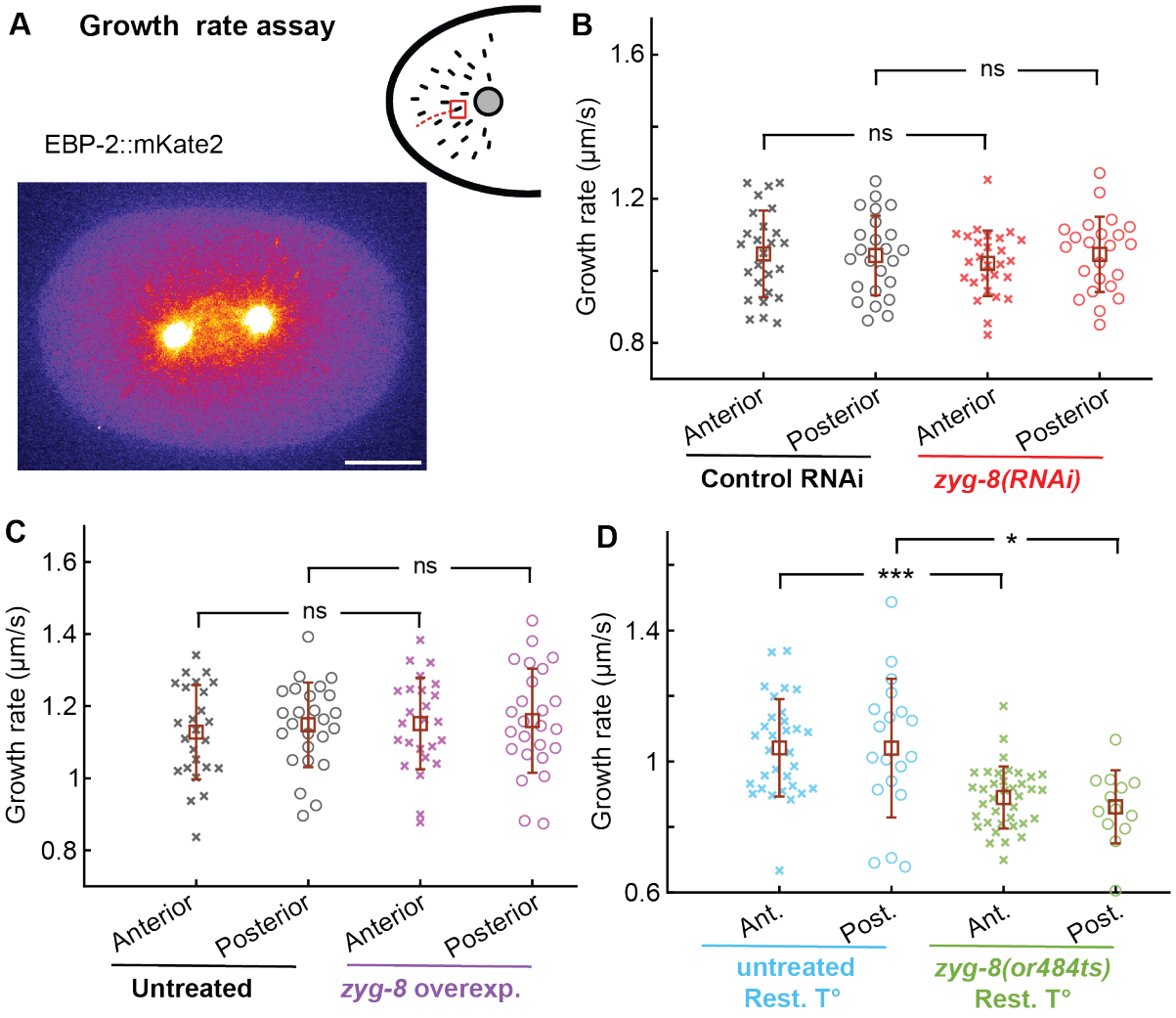


**Figure 2: In *zyg-8* mutants, microtubule growth rate is reduced by 15%.**
(**A**) Microtubule growth rate assay by tracking comets in embryos whose microtubule plus-ends were fluorescently labelled with EBP-2::mKate2 (Method M8). Example of a control RNAi embryo processed with Kalman denoising, a preprocessing step performed prior to quantification. Scale bar represents 10 µm. (**B-D**) Growth rates of astral microtubules measured at (cross) anterior and (circle) posterior centrosomes: (B) (red) *N* = 27 comets from anterior centrosome and *N* = 23 comets from posterior centrosome in 10 *zyg-8(RNAi)*-treated embryos, and (black) *N* = 26 comets from anterior centrosome and *N* = 24 comets from posterior centrosome in 8 control RNAi embryos; (C) (purple) *N* = 25 comets from anterior centrosome and *N* = 25 comets from posterior centrosome in 10 *zyg-8* overexpressing embryos and (black) *N* = 25 comets from anterior centrosome and *N* = 25 comets from posterior centrosome in 10 untreated embryos; (D) (light green) *N* = 37 comets from microtubules emanating from the anterior centrosome and *N* = 13 comets from posterior centrosome in 10 *zyg-8(or484ts)* mutants, and (light blue) *N* = 31 comets from anterior-centrosome and *N* = 19 posterior-centrosome comets in 13 untreated embryos, both at the restrictive temperature (Rest. T°). The brown squares and error bars correspond to the means and SD. * and *** indicate significant differences with $1x10^{-3}$

< $p \leq 1x10^{-2}$ and $p \leq 1x10^{-4}$, respectively. ns denotes non-significant differences ($p > 0.05$) (Method M14).

We and others have shown that the characteristics of spindle-pole oscillations were sensitive to microtubule dynamics [25, 63]. Besides, a previous study has investigated microtubule growth and nucleation perturbations in *C. elegans* zygotes across a broad range of MAP depletions, including ZYG-8 [42]. This study found that ZYG-8 promotes microtubule growth, and limits microtubule nucleation, although its effects were weaker than that of the polymerase ZYG-9$^{XMAP215}$ and the nucleator SPD-2$^{CEP192}$. To further explore the functions of ZYG-8, we quantified both parameters in our three genetic perturbations. We used an EB-labelling of microtubule plus-ends to assess whether the astral microtubule growth rate was altered, (Method M8, Figure 2A). We detected no significant changes in growth rate in either *zyg-8(RNAi)*-treated embryos, for which depletion was partial (Figure S2B), or in those overexpressing *zyg-8* (Figure 2C). This suggested that the oscillation amplitude variations in these two perturbative conditions had an alternative origin. In *zyg-8(or484ts)* mutants at the restrictive temperature, we observed a significant 15% reduction in microtubule growth rate (Figure 2D), consistent with previous results using *zyg-8(RNAi)* by injection [42]. To test whether this 15% reduction in microtubule growth could account for the exaggerated spindle-pole oscillations observed in *zyg-8* mutants, we performed a partial RNAi depletion of the microtubule polymerase ZYG-9$^{XMAP215}$ [42, 75, 76]. As expected, this treatment resulted in a shorter mitotic spindle [75] (Figure S4A) and a 16% reduction in microtubule growth rate, comparable to that observed in *zyg-8* mutants (Figure S4B). However, spindle-pole oscillation amplitudes and frequencies were either unaffected or slightly reduced, and did not phenocopy *zyg-8* mutant phenotype (Figure S4C, D). These results suggested that the limited contribution of ZYG-8 in promoting microtubule growth was not sufficient to account for its critical function in regulating spindle dynamics during anaphase.

Alternatively, ZYG-8 has been proposed to limit microtubule nucleation in the *C. elegans* zygote [42]. To test this, we estimated the nucleation rate of astral microtubules under our three genetic perturbation conditions. Specifically, we counted comet-like structures representing EBP-2::mKate2 labelled plus-ends of growing microtubules emanating from centrosomes (Method M8, Figure 3A). We observed a significant increase in the nucleation rate in *zyg-8(or484ts)* mutants and a decrease upon *zyg-8* overexpression, whereas *zyg-8(RNAi)* had no significant effect (Figure 3B-D). Since centrosome diameter correlates with nucleation capacity [77-79], we also measured centrosome size using mCherry::TBG-1 (Method M9, Figure 3E, F). We found statistically significant differences in centrosome diameter, with a 12% decrease upon *zyg-8* overexpression (Figure 3G) and a 6% increase following *zyg-8(RNAi)* treatment (Figure 3H). These results collectively indicated that ZYG-8 functions to restrict microtubule nucleation. Next, we tested whether altered nucleation alone could explain the spindle-pole oscillation phenotype observed upon *zyg-8* perturbation. To this end, we partially depleted SPD-2$^{CEP192}$ by RNAi to reduce microtubule nucleation and assessed the effects on spindle pole oscillations [80]. *spd-2(RNAi)* caused a 21% reduction in centrosome diameter (Figure S5A, B). This perturbation was more pronounced than that seen with either *zyg-8* overexpression or RNAi (Figure 3G, H). Concurrently, spindle-pole oscillation amplitudes were not significantly affected (Figure S5C). Besides, unlike embryos overexpressing *zyg-8* showing a significant 20% increase in oscillation frequency, *spd-2(RNAi)*-treated embryos exhibited only an 11% decrease in frequency (Figure S5D). Together, these

findings suggested that ZYG-8's role in limiting microtubule nucleation alone did not account for the anaphase spindle oscillation phenotypes observed upon targeting *zyg-8*.

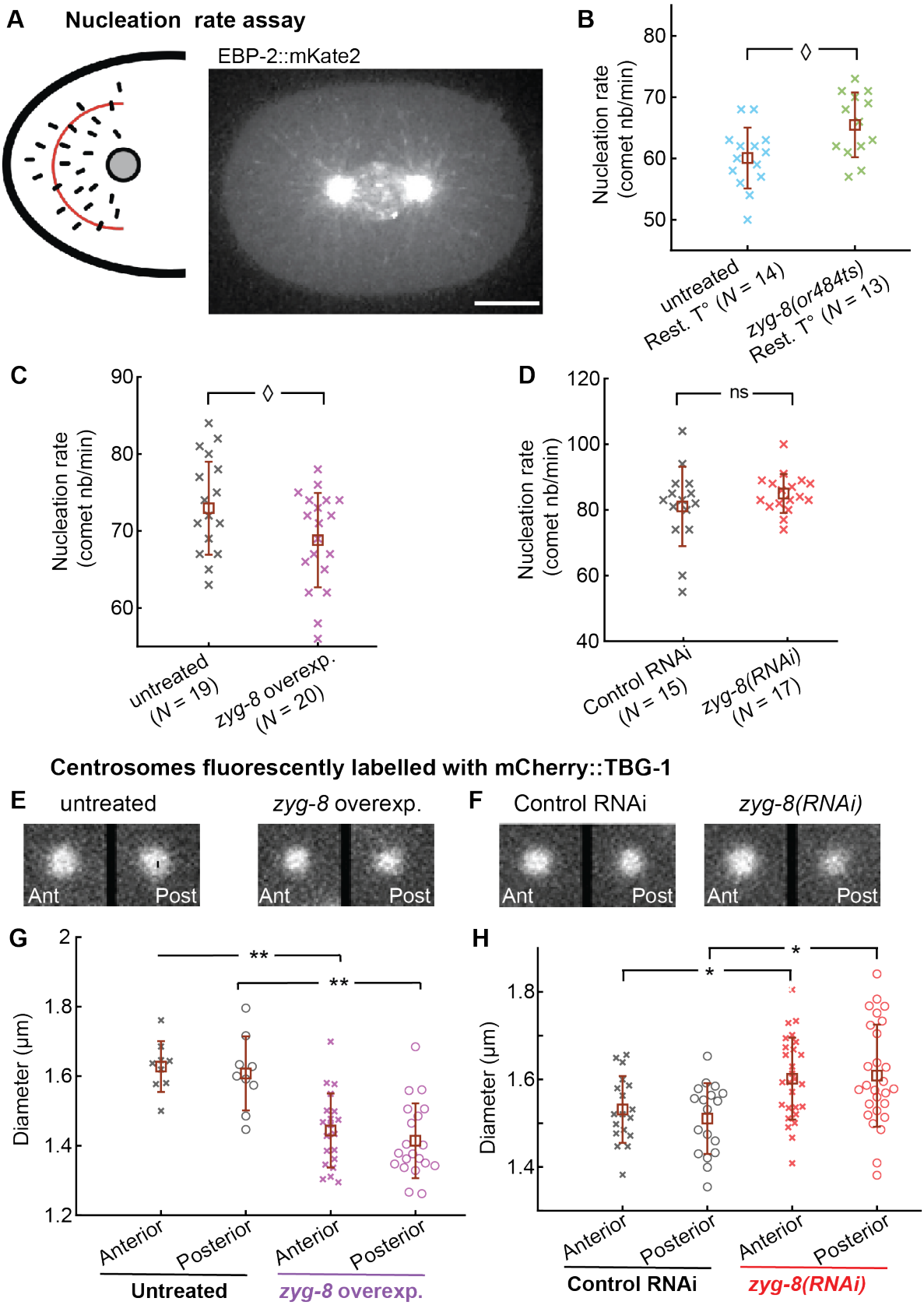

**Figure 3: ZYG-8 limits microtubule nucleation.**
(**A**) Microtubule nucleation rate assay by counting comets crossing a half-circle region of interest positioned 9 μm from the centrosome in embryos whose microtubule plus-ends were fluorescently labelled using EBP-2::mKate2 (Method M8). Example of a control RNAi embryo processed with Candle denoising, a preprocessing step performed prior to comet counting. Scale bars represent 10 μm. **(B-D)** Nucleation rates of the astral microtubules with *N* indicating the number of analysed centrosomes per condition: (A) (light green) $N_e$ = 8 *zyg-8(or484ts)* mutants and (light blue) $N_e$ = 9 untreated embryos, both at the restricted temperature (Rest. T°); (B) (purple) $N_e$ = 10 *zyg-8* overexpressing embryos and (black) $N_e$ = 10 untreated embryos; (C) (red) $N_e$ = 10 *zyg-8(RNAi)*-treated embryos and (black) $N_e$ = 8 control RNAi embryos. (**E-F**) Regions centred on the centrosomes (40 x 40 pixels; 6.4 x 6.4 μm) from exemplar microscopy images showing centrosomes fluorescently labelled with mCherry::TBG-1: (E) representative images of untreated and *zyg-8* overexpressing embryos; (F) representative images of control RNAi and *zyg-8(RNAi)*-treated embryos. **(G-H**) Diameters during metaphase of (cross) anterior and (circle) posterior centrosomes (Method M9): (G) (purple) $N_e$ = 21 *zyg-8* overexpressing embryos and (black) $N_e$ = 9 untreated embryos; (H) (red) $N_e$ = 27 *zyg-8(RNAi)*-treated embryos and (black) $N_e$ = 18 control RNAi embryos. The brown squares and error bars correspond to the means and SD. ◊, *, and ** indicate significant differences with $1x10^{-2} < p \leq 5x10^{-2}$, $1x10^{-3} < p \leq 1x10^{-2}$, and $1x10^{-4} < p \leq 1x10^{-3}$, respectively. ns denotes non-significant differences ($p > 0.05$) (Method M14).

## 2- Cortical microtubule dynamics do not support a role for ZYG-8 in microtubule stabilisation.

Previous works in human cells and *in vitro* have proposed that members of the Doublecortin family stabilise microtubules by preventing catastrophe and/or inhibiting depolymerisation [43, 81-83]. We investigated whether a similar regulatory mechanism operates in the *C. elegans* zygote. Inspired by a previous study in nematodes on the role of CLS-2$^{CLASP}$ in microtubule stability [84], we imaged, at the cell cortex, embryos expressing GFP::TBB-2 (*zyg-8(RNAi)* treatment) or mCherry::tubulin (*zyg-8* overexpression) and examined both the number and duration of astral microtubule contacts there (Figure 4A, B; Movies S1-S4). Since microtubule catastrophes are rare in *C. elegans* zygote cytoplasm, most astral microtubules grow until they reach the cortex [63, 85]. If ZYG-8 stabilises microtubules by limiting depolymerisation or preventing catastrophe in the cytoplasm, *zyg-8(RNAi)* would be expected to reduce the number of cortical contacts. However, we observed the opposite: *zyg-8(RNAi)* increased the number of cortical contacts by an average of 50%, while *zyg-8* overexpression led to a 13% reduction (Figure 4C, D). These results argued against a cytoplasmic stabilisation role for ZYG-8. Next, to explore whether ZYG-8 might stabilise microtubules at the cell cortex by reducing catastrophe frequency, we analysed the duration of microtubule cortical contacts. If ZYG-8 acted to stabilise microtubules at the cortex, *zyg-8(RNAi)* would be expected to increase the number of short-duration contacts. In contrast, *zyg-8(RNAi)* resulted in a 10-15% reduction in the short-duration contacts (Figure 4E, F). Conversely, *zyg-8* overexpression led to a 7% increase in short-duration contacts (Figure 4G, H). Altogether, these cortical measurements did not support a role for ZYG-8 in stabilising microtubules.

To further test this finding, we compared spindle oscillation phenotypes in *zyg-8(RNAi)*-treated embryos with those following depletion of either CLS-2$^{CLASP}$—a known microtubule stabiliser that prevents catastrophe and promotes rescue [84, 86]— or KLP-7$^{MCAK}$, which destabilises microtubules by promoting depolymerisation [87]. We validated the penetrance of each RNAi treatment by observing accelerated mitotic spindle elongation [88-90] (Figure S6A, D). Besides, metaphase spindle was longer upon *klp-7(RNAi)*, as expected [91] (Figure S6D). *cls-2(RNAi)* caused an increase in oscillation amplitude, although weakly significant, with

**Dynamics of astral microtubules at the cell cortex of *C. elegans* zygote**

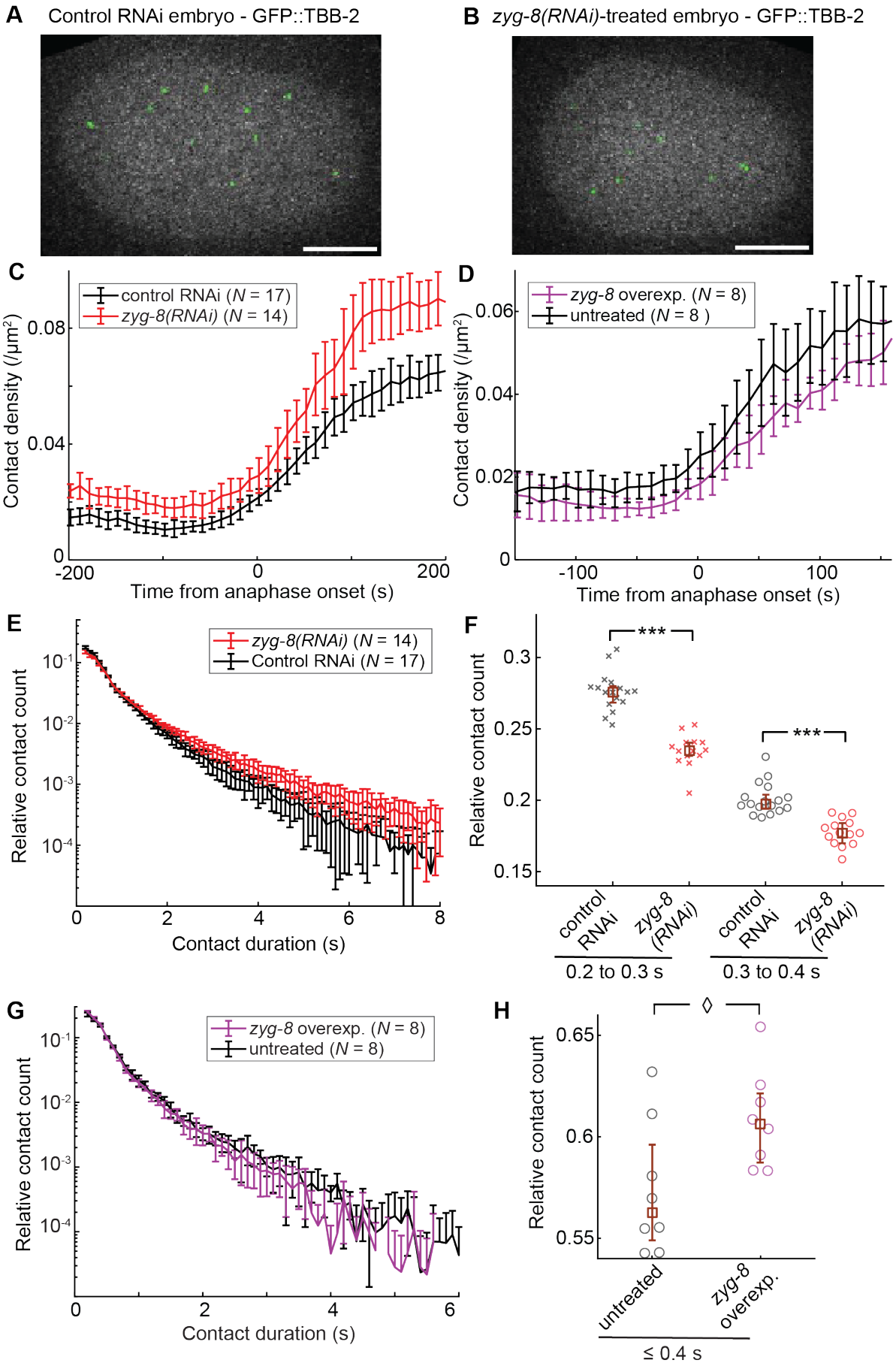

**Figure 4: Perturbations in microtubule cortical dynamics upon targeting *zyg-8* do not support a role for ZYG-8 in stabilising microtubules.**
(**A-B**) Embryos whose microtubules are labelled by GFP::TBB-2 and imaged at the cortical plane (Method M4): examples of (A) a control RNAi embryo (Movie S1), and (B) a *zyg-8(RNAi)*-treated embryo (Movie S2) at anaphase onset. Green spots highlight the detected contacts (Method M10). Scale bars represent 10 μm. (**C-D**) Embryo-averaged density of astral microtubule contacts at the cortex plane along mitosis. We tracked and analysed the cortical contacts of microtubules labelled: (C) by GFP::TBB-2 in (red) $N$ =14 *zyg-8(RNAi)*-treated embryos and (black) $N$ = 17 control RNAi ones; (D) by mCherry::tubulin in (purple) $N$ = 8 *zyg-8* overexpressing embryos and (black) $N$ = 8 untreated ones. (**E**) Embryo-averaged distributions of cortical lifetimes of astral microtubules during metaphase (Kolmogorov–Smirnov test: $p = 6\text{x}10^{-4}$, Methods M10 and M14). Embryos are the same as in panel C. (**F**) Relative contact counts for the two shortest duration bins (0.2 to 0.3 s & 0.3 to 0.4 s) from the distributions presented in panel E, highlighting differences in brief contact durations. (**G**) Embryo-averaged distributions of cortical lifetimes of astral microtubules during metaphase (Kolmogorov–Smirnov test: $p$ = 0.18, Methods M10 and M14). Embryos are the same as in panel D. (**H**) Relative counts of contacts with durations below 0.4 s, highlighting variations in short-lived durations. Data were derived from the distributions in panel G. Representative movies of each of the four present conditions are provided as Movies S1-S4. Microtubule contacts were tracked using u-track (Method M10). The brown squares and error bars correspond to the medians and the quartiles. ◊ and *** indicate significant differences with $1\text{x}10^{-2} < p \leq 5\text{x}10^{-2}$ and $p \leq 1\text{x}10^{-4}$, respectively (Method M14).

no significant variation in oscillation frequency (Figure S6B, C). These phenotypes were distinct from those observed upon *zyg-8(RNAi)*, which led to a major amplitude increase and a frequency decrease. KLP-7 depletion increased oscillation amplitudes at the posterior centrosome and decreased frequencies at both centrosomes (Figure S6E, F). If ZYG-8 stabilised microtubules by preventing depolymerisation, we would have observed an oscillation phenotype opposite to that of KLP-7 depletion. This was not the case. We concluded that a putative role of ZYG-8 in stabilising the microtubules could not account for the observed phenotypes.

Overall, we concluded that the perturbations of spindle-pole oscillations and microtubule dynamics at the cell cortex when we targeted *zyg-8*, could not be explained solely by alterations in microtubule dynamics. Interestingly, proteins of the Doublecortin family have been proposed to regulate microtubule rigidity in neurons [34, 92]. We asked whether the observed perturbations in spindle-pole oscillations and cortical microtubule behaviour could result from altered microtubule rigidity upon targeting *zyg-8*.

### 3- ZYG-8 would control microtubule flexural rigidity.

Direct measurements of microtubule rigidity in *C. elegans* embryos are not feasible, as standard techniques (e.g., thermal fluctuations, optical trap/tweezers, or calibrated flow) require isolated microtubules [15-17, 32, 93-95]. As a quantitative alternative, we employed a set of complementary metrics that collectively capture different aspects of microtubule bending behaviour (Method M11). First, we analysed local curvature distributions, a method previously used as a proxy for rigidity under the assumption that the forces acting on the microtubule network are similar between conditions [20, 96, 97]. In this context, a higher proportion of strongly curved segments reflects reduced rigidity (Figure S7A). To complement this population-level analysis with a more filament-specific readout, we extracted the 95$^{th}$ percentile of curvature values along individual microtubules, as a robust measure of maximum

bending per microtubule (Figure S7B). Finally, we incorporated filament tortuosity—a global shape descriptor independent of curvature computation and less sensitive to sampling resolution. Defined as the ratio between curvilinear and end-to-end distances, tortuosity has also been used previously [33] (Figure S7C).

**A Live *zyg-8(or484ts)* mutant at the restrictive temperature with GFP::TBB-2 labelling**

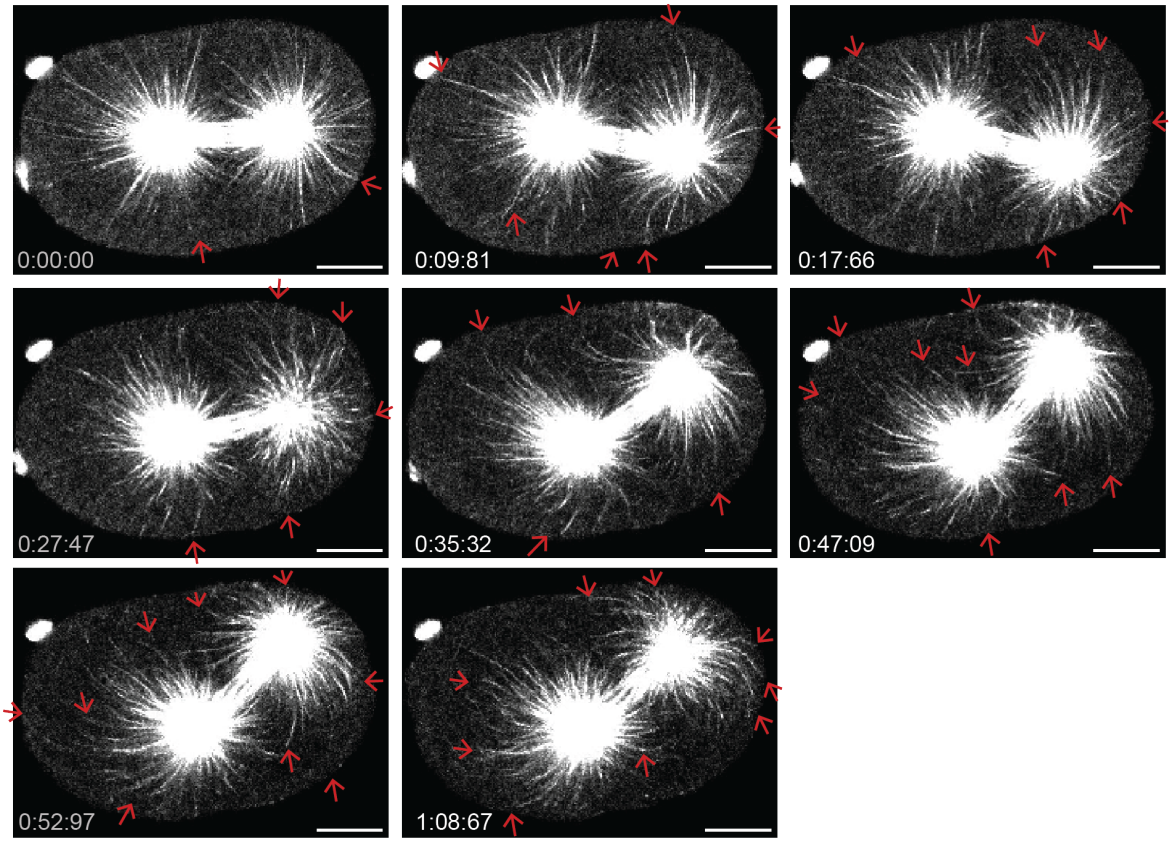


**B Live untreated embryo at the restrictive temperature with GFP::TBB-2 labelling**

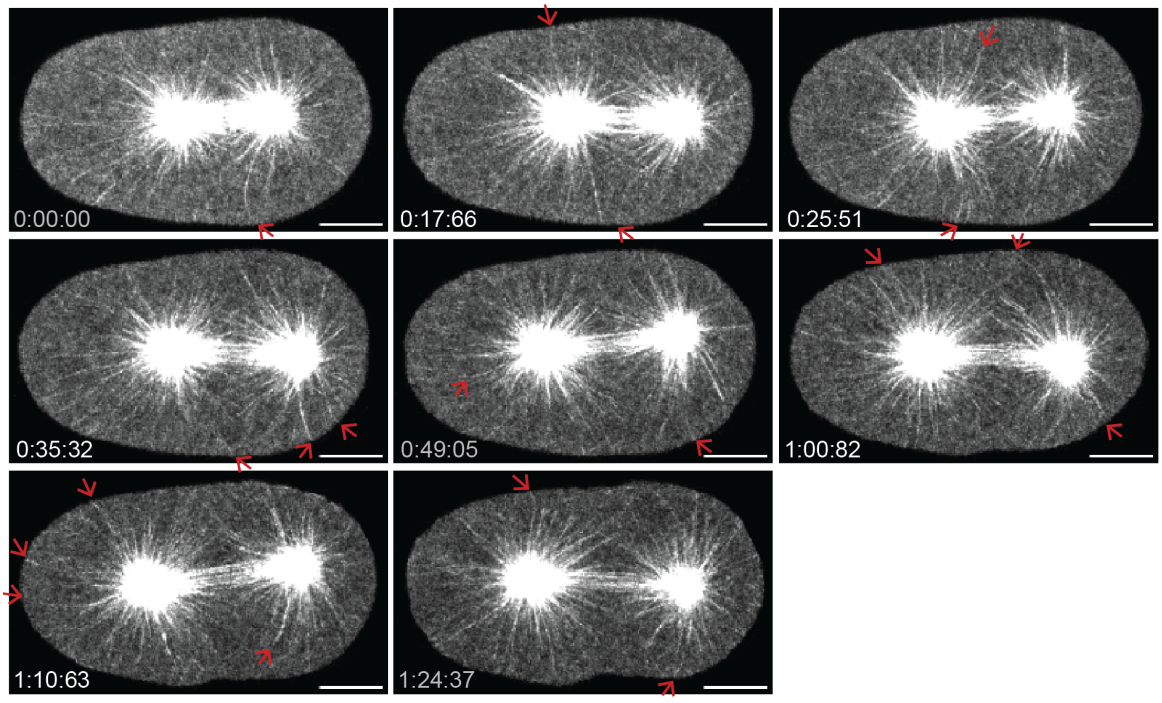

**Figure 5**: **In *zyg-8(or484ts)* mutants, astral microtubules are highly bent during the exaggerated spindle pole oscillations.**
Time-lapse confocal super-resolved images along anaphase of (**A**) an exemplar *zyg-8(or484ts)* mutant and (**B**) an exemplar untreated embryo, both at the restrictive temperature. Microtubules were labelled by GFP::TBB-2. Time is indicated from first image in mm:ss:ms. Scale bars represent 10 μm. These time-lapse images are sourced from the movies S5 and S7. Red arrows highlight bent microtubules.

A previous study showed that microtubules in axonal growth cones were more often strongly curved upon depletion of the Doublecortin-family proteins DCX and DCLK1. Similarly, we asked whether astral microtubules displayed increased local curvature in *zyg-8(or484ts)* mutants. We imaged live embryos expressing GFP::TBB-2 using a super-resolved confocal microscope (Nikon with Nsparc detector, Method M4). We observed regions of high local curvatures along astral microtubules, which appeared more frequently in the mutants (Figure 5A, Movies S5 and S6) than in untreated embryos (Figure 5B and Movie S7), both at the restrictive temperature. Besides, astral microtubules in the mutants were long and extended to the cell periphery. The fast motion of astral microtubules required high image acquisition rate to avoid motion blur, which led, unfortunately, to images with low signal-to-noise ratio complicating microtubule curvature quantification. In *zyg-8(or484ts)* mutants, significant out-of-plane movements hindered microtubule visualisation along their full length, calling for acquisitions on multiple z-sections (Movies S5 & S6). As a result, we opted for investigating curvature phenotypes in fixed samples.

We imaged microtubules stained for α-tubulin using a confocal super-resolution microscopy (Methods M3 and M4). In *zyg-8(RNAi)*-treated fixed embryos, we observed more bent astral microtubules (Figure S7D). This phenotype was even more pronounced in *zyg-8(or484ts)* fixed mutants at the restrictive temperature, where microtubule curvatures were noticeably increased (Figure S7E). We also detected fragmented microtubules in the cytoplasm of some fixed mutant embryos (Figure S7E). Interestingly, such fragmentation may result from excessive curvatures, as previous studies have linked microtubule breakage to strong bending [96, 98, 99]. Fragmentation could also contribute to the appearance of shorter astral microtubules. This phenotype—very-short astral-microtubule—was observed only in a subset of *zyg-8(or484ts)* fixed mutants, resembling the initial images of stained microtubules in this mutant [48, 72].

To go beyond qualitative visual inspection, we quantified the distribution of microtubule curvatures. Accurate segmentation was essential for this analysis but proved challenging due to faint and uneven microtubule labelling. To overcome this, we assembled a five-step image processing pipeline enabling the segmentation of astral microtubules and computation of local curvatures on a pixel-by-pixel basis using a three-point method (Figure S8, Method M11). By averaging curvature distributions across conditions, we observed a slight decrease in the proportion of low local curvatures following *zyg-8(RNAi)* treatment (Figure 6A, B). In *zyg-8(or484ts)* mutants at the restrictive temperature, the distribution shifted significantly further toward higher curvature values compared to controls, showing a stronger effect than RNAi (Figure 6C, D). Notably, some local curvature values reached up to 0.8 $\mu m^{-1}$, consistent with curvature thresholds associated with microtubule breakage [98, 99]. Focussing on the highest curvatures, we observed increases of 13% in metaphase and 12% in anaphase following *zyg-8(RNAi)*. These increases were further amplified in *zyg-8(or484ts)* mutants, reaching 33% and

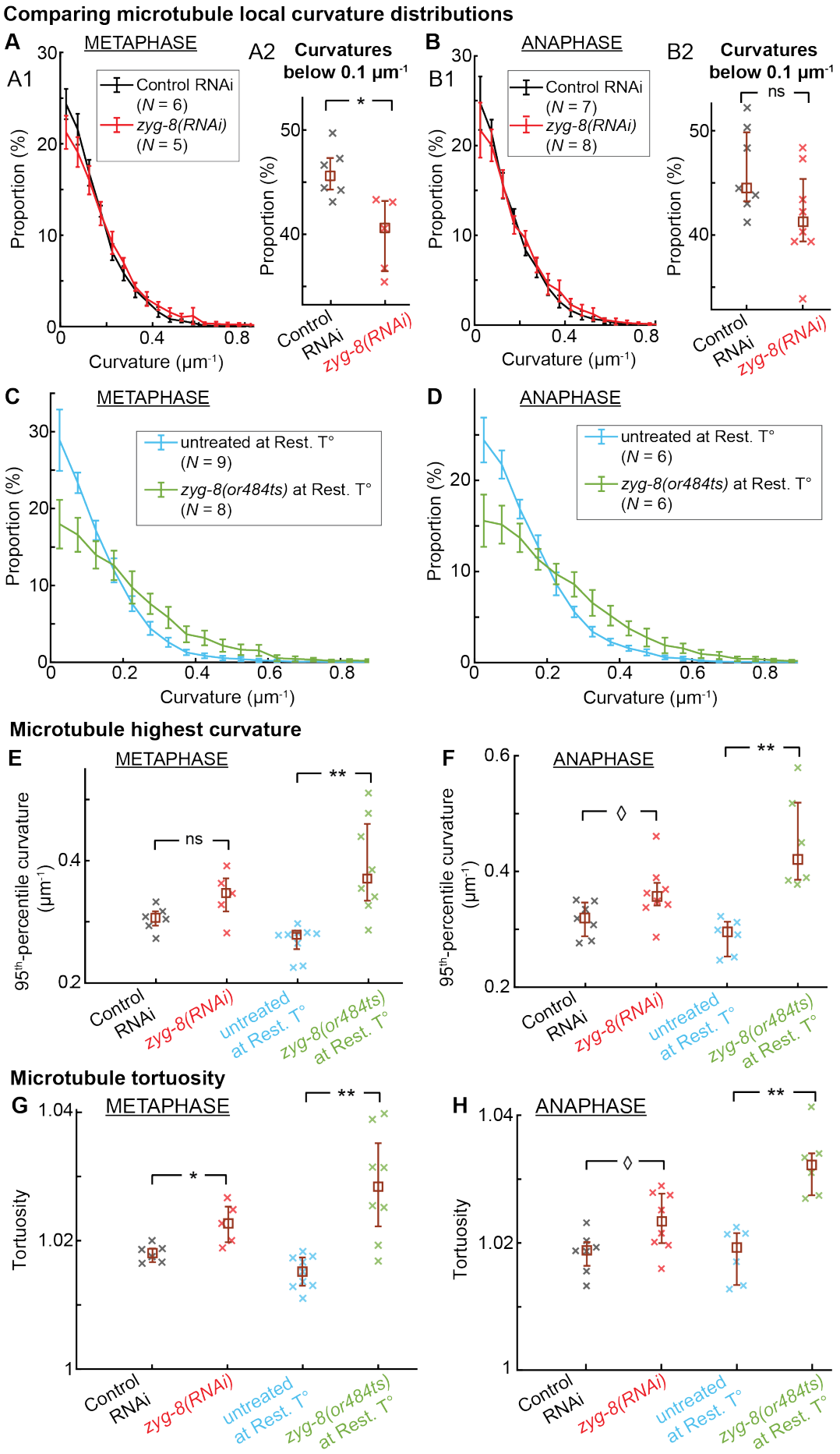
Comparing microtubule local curvature distributions
A
METAPHASE
A1
Control RNAi (N = 6)
zyg-8(RNAi) (N = 5)
Proportion (%)
Curvature (µm-1)
A2
Curvatures below 0.1 µm-1
*
Control RNAi
zyg-8(RNAi)
B
ANAPHASE
B1
Control RNAi (N = 7)
zyg-8(RNAi) (N = 8)
B2
ns
C
METAPHASE
untreated at Rest. T° (N = 9)
zyg-8(or484ts) at Rest. T° (N = 8)
D
ANAPHASE
untreated at Rest. T° (N = 6)
zyg-8(or484ts) at Rest. T° (N = 6)
Microtubule highest curvature
E
METAPHASE
95th-percentile curvature (µm-1)
ns
**
Control RNAi
zyg-8(RNAi)
untreated at Rest. T°
zyg-8(or484ts) at Rest. T°
F
ANAPHASE
◊
Microtubule tortuosity
G
METAPHASE
Tortuosity
H
ANAPHASE

**Figure 6: Astral microtubules appear more curved and tortuous in *zyg-8(RNAi)*-treated embryos, and even more so in *zyg-8(or484ts)* mutants.**
(**A-B**) Embryo-averaged distributions of astral microtubule local curvatures of (red) *zyg-8(RNAi)*-treated embryos and (black) control RNAi embryos: (A1) during metaphase with (red) $N = 5$ z-projected stacks and (black) $N = 6$ z-projected stacks (Kolmogorov–Smirnov test: $p = 0.36$, Method M14); and (B1) during anaphase with (red) $N = 8$ z-projected stacks and (black) $N = 7$ z-projected stacks (Kolmogorov–Smirnov test: $p = 0.36$, Method M14). (A2, B2) Focus on the proportions of low local curvatures ($\leq 0.01\ \mu m^{-1}$) for the same embryos as in panels A1 & B1. **(C-D)** Embryo-averaged distributions of astral microtubule local curvatures of (light green) *zyg-8(or484ts)* mutants and (light blue) untreated embryos, both at the restrictive temperature: (C) during metaphase with (light green) $N = 8$ z-projected stacks and (light blue) $N = 9$ z-projected stacks (Kolmogorov–Smirnov test: $p = 0.03$, Method M14); and (D) during anaphase with (light green) $N = 6$ z-projected stacks and (light blue) $N = 6$ z-projected stacks (Kolmogorov–Smirnov test: $p = 0.014$, Method M14). (**E-F**) Medians per z-projected stack of the highest curvatures (measured as 95$^{th}$ percentile curvature): (E) during metaphase (data are the same as in panels A & C); and (F) during anaphase (same data as in panels B & D). (**G-H**) Medians per z-projected stack of microtubule tortuosity: (G) during metaphase, using the same embryos as in panels A, C & E; and (H) during anaphase, using the same embryos as in panels B, D & F. Embryos were fixed and immuno-stained for $\alpha$-tubulin; microtubules were segmented; and local curvature and tortuosity were computed (Methods M3, M4, M11). The brown squares and error bars correspond to the medians and the quartiles. ◊, *, and ** indicate significant differences with $1x10^{-2} < p \leq 5x10^{-2}$, $1x10^{-3} < p \leq 1x10^{-2}$, and $1x10^{-4} < p \leq 1x10^{-3}$, respectively. ns denotes non-significant differences ($p > 0.05$) (Method M14).

42% in metaphase and anaphase, respectively (Figure 6E, F). Lastly, microtubule tortuosity was significantly elevated following *zyg-8(RNAi)* treatment, and increased even further in *zyg-8(or484ts)* mutants at the restrictive temperature (Figure 6G, H). Together, these analyses demonstrated that ZYG-8 modulates microtubule curvature and tortuosity, supporting its role in regulating microtubule flexural rigidity.

We foresaw that reduced rigidity would lead to increased bending, resulting in weaker pushing forces against the cortex. This, in turn, would delay force-dependent catastrophes and increase the cortical lifetimes of astral microtubules [100, 101] (Figure 7A). We used the established agent-centred simulation *Cytosim* [102] to test this hypothesis (Table S2, Method M12). We conducted three sets of simulations in which only the rigidity of astral microtubules was varied, using values of 2, 10, and 25 $pN.\mu m^2$ (Movies S8-S10, Figure S9A). These values were based on *in vitro* measurements of microtubule rigidity [15-17, 93, 95]. We found that these *in silico* changes in rigidity affected both microtubule curvature and tortuosity. Specifically, the highest curvatures and tortuosity increased as rigidity decreased (Figure S9B, C). Importantly, microtubules with lower rigidity exhibited longer cortical lifetimes, supporting our initial prediction (Figure S9D). Returning to *in vivo* experiments, we measured the cortical contact durations of astral microtubules in *zyg-8(RNAi)*-treated embryos expressing GFP::TBB-2 and found an increased proportion of microtubules with prolonged contacts compared to control RNAi embryos (Figure 4E). This observation was consistent with reduced microtubule rigidity in *zyg-8(RNAi)*-treated embryos.

Finally, we investigated spindle pole oscillations in light of ZYG-8's role in microtubule rigidity. We previously proposed an antagonistic-motors model to explain these oscillations, in which the oscillation frequency is in particular proportional to the square root of the centring rigidity [57]. This centring rigidity has been associated with the pushing force generated by

microtubules growing against the cortex [25, 68]. Consequently, lower microtubule rigidity—leading to reduced pushing force—was expected to lower centring rigidity, and thus decrease oscillation frequency. Indeed, we observed a reduction in oscillation frequency in *zyg-8(RNAi)*-treated embryos (Figure 1D). Conversely, this frequency was increased in embryos overexpressing *zyg-8* (Figure 1D).

Taken together, these three experiments supported a model in which ZYG-8 contributes to microtubule stiffening.

### 4- ZYG-8 ensures spindle centring mostly by controlling microtubule rigidity.

Although the centring force generated by microtubules pushing against the cell cortex—critically dependent on microtubule rigidity—was mostly invoked in metaphase [25, 27, 71], it is also thought to act as a restoring force for spindle rocking in anaphase [57, 60]. Indeed, we previously proposed that, when a spindle pole moves toward one side of the cortex, the centring spring opposes this displacement [57]. Consequently, a reduction in microtubule rigidity would decrease the stiffness of this centring spring, allowing greater spindle pole displacement and thereby increasing oscillation amplitudes (Figure 8E). In *zyg-8(RNAi)* condition or in *zyg-8(or484ts)* mutants, we observed a large increase in the amplitudes of spindle pole oscillations (Figure 1C). We therefore considered two possible and non-mutually exclusive explanations for this increase: enhanced cortical pulling or reduced cortical pushing.

To distinguish between these possibilities, we first measured the most posterior position of the posterior centrosome during anaphase following *zyg-8(RNAi)* treatment. We found no significant difference compared to controls (80.7 $\pm$ 1.4 % for *zyg-8(RNAi)* (*N* = 16), versus 79.8 $\pm$ 1.0 % for control RNAi embryos (*N* = 10), Student's *t*-test: *p* = 0.07)). This suggested that posterior displacement, driven by cortical pulling forces, remained largely unaltered. Next, we applied the DiLiPop analysis to assess cortical pulling and pushing events during anaphase. We previously showed that two populations of astral microtubules reside at the cell cortex, based on a statistical analysis of cortical contact durations [71] (Method M10). By genetically perturbing either pulling or pushing cortical forces, we associated the short-lived population with pulling events and the long-lived population with pushing [71]. Upon *zyg-8(RNAi)*, we observed a 10% rise in the lifetime of the pushing events (Figure 7B) and a 3% reduction in their density (Figure 7C). Since all cortical force generators are engaged in pulling during anaphase, this reduced density likely reflected the prolonged duration of individual pulling events [57, 63, 66]. These modest changes in pulling events could not account for the strong increase in oscillation amplitudes. We therefore concluded that *zyg-8(RNAi)* had only a minor effect on cortical pulling forces. In contrast, we found that pushing microtubules resided at the cortex significantly longer upon *zyg-8(RNAi)*, with a 37% increase in lifetimes (Figure 7D). This was consistent with their sensitivity to microtubule rigidity (Figure 7A). Besides, the density of pushing events increased by 22% (Figure 7E), partially due to an enhanced microtubule nucleation capacity (Figure 3F). Despite the rise in pushing event density, we proposed a global reduction in effective cortical pushing force, since a bent microtubule has a limited pushing force (Euler force). Consequently, the larger oscillation amplitudes observed following *zyg-8(RNAi)* treatment likely resulted from reduced pushing force, while cortical pulling forces appeared to be largely unaffected.

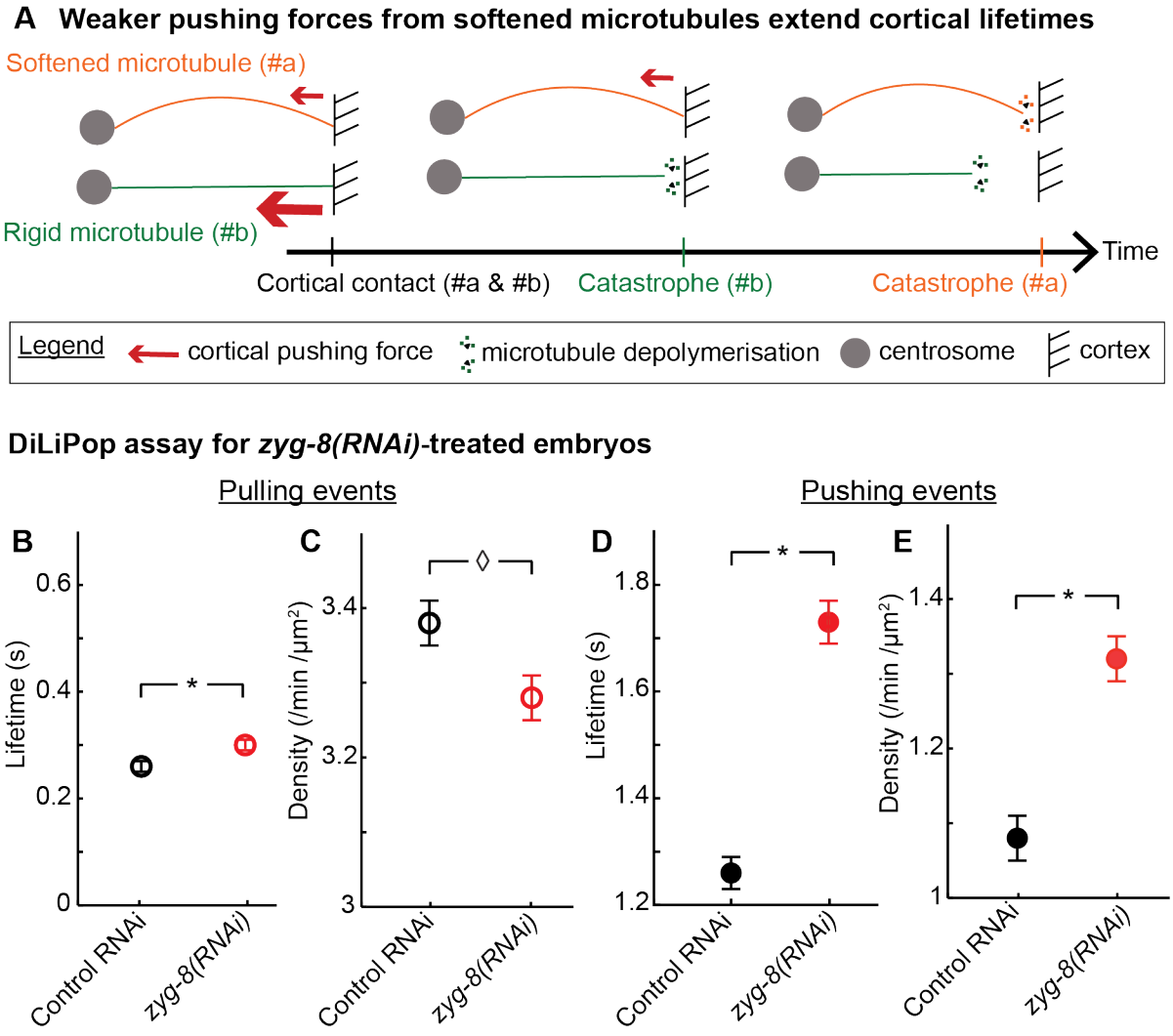


**Figure 7: Depleting ZYG-8 weakens highly the cortical pushing events.**
(**A**) Diagram illustrating the correlation between microtubule rigidity and cortical lifetime: (orange) softened microtubules lead to increased pushing-event lifetimes compared to (green) rigid microtubules, due to weaker pushing force (red arrow) delaying catastrophe. (**B**) Lifetimes and (**C**) densities of the cortical pulling events, and (**D**) lifetimes and (**E**) densities of the cortical pushing events during anaphase. We tracked and analysed the microtubule contacts at the cell cortex using a GFP::TBB-2 fluorescent labelling in (red) $N = 14$ *zyg-8(RNAi)*-treated embryos and (black) $N = 17$ control RNAi embryos (same embryos as for Figure 4C, E & F) (Method M10). ◊ and * indicate significant differences with $1x10^{-2} < p \leq 5x10^{-2}$ and $1x10^{-3} < p \leq 1x10^{-2}$, respectively (Method M14).

To further investigate the role of ZYG-8 in controlling microtubule rigidity—and, in turn, the centring force—we sought an alternative characterisation of spindle positioning forces at the cellular level. To do this, we used an assay previously developed by the team focussing on the spindle positional micro-movements acquired at high frame rate. We extracted the mechanical fingerprint of these micro-movements along the transverse axis during anaphase and fitted a second-order model to the experimental spectrum [25] (Method M13). Our analysis revealed that ZYG-8 depletion caused a large 79% reduction in the centring-to-damping corner frequency $f_c$, compared to the control (Table 1). We also observed a 24% decrease in the diffusion coefficient $D$, which scales inversely with damping, and a 35%

increase in the damping-to-inertia frequency $f_0$ (Table 1). We interpreted the decrease in $f_c$ as primarily reflecting a centring force reduction due to softer microtubules [25]. The moderate decrease in *D* likely resulted from an increased number of microtubules contacting the cortex. The rise in $f_0$ could be partly attributed to the reduced *D*, and appeared inconsistent with any notable increase in inertia, suggesting that the pulling forces were only mildly or not significantly affected. Overall, the mechanical fingerprint of spindle positioning following *zyg-8(RNAi)* treatment was qualitatively consistent with a reduction in the centring force, mainly due to softer microtubules. This reduction likely contributed to the increased amplitude of spindle pole oscillations.

In *zyg-8(or484ts)* mutants at the restrictive temperature, we observed larger amplitudes of spindle-pole oscillation amplitudes compared to those seen with *zyg-8(RNAi)* treatment (Figures 1C, S3). We hypothesised that this phenotype was due to a severely weakened centring force caused by excessively soft microtubules. This was supported by the increased proportion and magnitude of microtubule curvatures observed in these mutants (Figures 5 and 6). To test this hypothesis, we analysed spindle positional micro-movements in *zyg-8(or484ts)* mutants. We found a very large and significant reduction in the centring-to-damping corner frequency $f_c$, while the other two mechanical parameters, *D* and $f_0$, were not significantly altered (Table 1). These results suggested that in *zyg-8(or484ts)* mutants, the pronounced reduction in $f_c$, indicative of weakened centring forces, accounted for the exaggerated spindle pole oscillations. This reduction was likely due to decreased microtubule rigidity, consistent with the observed abnormalities in microtubule shapes.

| **Conditions** | **Frequency interval** | ***D* ($m^2/s$)** | **$f_c$ (Hz)** | **$f_0$ (Hz)** |
|---|---|---|---|---|
| Control RNAi (*N* = 15) | 0.03 -> 0.3 Hz | $1.7 \times 10^{-13}$ [$0.7 - 15.0 \times 10^{-13}$] | 0.86 [0.03 - 6.68] | $3.1 \times 10^{-3}$ [$0.4 - 51.4 \times 10^{-3}$] |
| *zyg-8(RNAi)* (*N* = 20) | | $1.3 \times 10^{-13}$ [$0.7 - 166 \times 10^{-13}$] | 0.18 [0.13 - 5.78] | $4.2 \times 10^{-3}$ [$0.1 - 7.4 \times 10^{-3}$] |
| *ptl-1(RNAi)* (*N* = 13) | | $1.0 \times 10^{-13}$ [$0.8 - 4.9 \times 10^{-13}$] | 0.34 [0.09 - 5.46] | $5.9 \times 10^{-3}$ [$0.1 - 83.3 \times 10^{-3}$] |
| Untreated at the restrictive temperature (*N* = 11) | 0 -> 0.5 Hz | $7.3 \times 10^{-14}$ [$5.8 - 9.0 \times 10^{-14}$] | 0.19 [0.15 - 0.22] | $1.3 \times 10^{-2}$ [$1.1 - 1.5 \times 10^{-2}$] |
| *zyg-8(or484ts)* at the restrictive temperature (*N* = 12) | | $11.3 \times 10^{-14}$ [$6.2 - 687.9 \times 10^{-14}$] | $0.9 \times 10^{-3}$ [$0.89\ 0.95 \times 10^{-3}$] | $1.3 \times 10^{-2}$ [$0.01 - 2.4 \times 10^{-2}$] |

**Table 1: Targeting *zyg-8* or *ptl-1* reduces the centring frequency.**
Mechanical parameters measured during anaphase, including the diffusion coefficient (*D*) and two corner frequencies ($f_c$ and $f_0$). They were obtained by fitting the experimental power spectra of spindle positional micromovements along the transverse axis within the specified frequency interval using a second-order model (Method M13). The confidence intervals were estimated using the bootstrap resampling method with a significance level of 0.05.

To further address the role of microtubule rigidity in contributing to spindle centring, we targeted another protein known to regulate microtubule flexural rigidity in neurons and asked whether similar perturbations in spindle choreography could be reproduced. We depleted PTL-1, the sole nematode homolog of the Tau protein family, using RNAi [103, 104]. This led to maximal amplitude increases of 34% at the anterior pole and 13% at the posterior pole, as well as frequency decreases of 9% and 11%, respectively—both consistent with reduced microtubule rigidity (Figure S10). Besides, analysis of spindle positional micro-movements along the transverse axis during anaphase revealed a 60% reduction in the centring-to-damping corner frequency $f_c$ (Table 1). These results resembled those obtained with *zyg-8(RNAi),* suggesting a decrease in centring forces, although to a lesser degree. The milder phenotypes observed in *ptl-1(RNAi)* embryos were likely due to lower *ptl-1* expression levels in the zygote compared to *zyg-8* [105].

Altogether, our findings demonstrated that ZYG-8 regulates the cortical pushing force responsible for spindle centring, primarily by modulating microtubule flexural rigidity. This pushing force acted as a restoring force during anaphase spindle rocking. While cortical pulling forces remain the dominant drivers of spindle posterior displacement, our work highlighted the important, though often underappreciated, contribution of pushing forces to overall spindle choreography.

### 5- Very soft microtubules disrupt final spindle positioning and orientation.

Having identified an additional role for ZYG-8 in controlling microtubule flexural rigidity, we next investigated the importance of this function for successful asymmetric mitosis. In *zyg-8(or484ts)* mutants at the restrictive temperature, the enhanced spindle-pole oscillation amplitudes – greater than those observed in *zyg-8(RNAi)* – resulted in a significantly reduced centrosome-to-cortex distance (Figure S3B). We thus examined the consequences of this reduced distance in the course of anaphase. In untreated embryos, spindle oscillations gradually built up and then died down, ultimately leaving the spindle properly aligned along the anteroposterior (AP) axis of the embryo (Figure 8A). In contrast, in *zyg-8(or484ts)* mutants, the closer proximity of the centrosome to the cell cortex pulled the entire spindle further toward the cell periphery. This appeared to prevent the spindle from re-centring during the oscillation die-down (Figure 8B). The reduction in cortical pushing disrupted the force balance, favouring excessive net pulling. As a result, the spindle failed to return to the central position by the end of anaphase, leading to both mispositioning and misorientation (Figure 8B-D). Notably, embryonic lethality of *zyg-8(or484ts)* mutants was elevated (> 99%) at the restrictive temperature. Based on these observations, we proposed that the spindle misalignment seen in *zyg-8(or484ts)* mutants arose from impaired pushing forces, which disturbed the balance between pulling and pushing forces required for proper spindle positioning.

We hypothesised that reducing cortical pulling force could rescue the final spindle orientation in *zyg-8(or484ts)* mutants, by preventing an excessive imbalance between cortical pulling and pushing forces. To test this, we depleted GPR-1/2$^{LGN}$ by RNAi, a component of the cortical force generator that pulls on astral microtubules. In non-mutated embryos treated with *gpr-1/2(RNAi)* at the restrictive temperature, we observed no spindle pole oscillations, and the most-posterior position of the spindle was significantly shifted toward the cell centre, consistent with a decrease in cortical pulling forces (Figure S11A). Similarly, in *zyg-8(or484ts)* mutants treated with *gpr-1/2(RNAi)* at the restrictive temperature, oscillations were absent

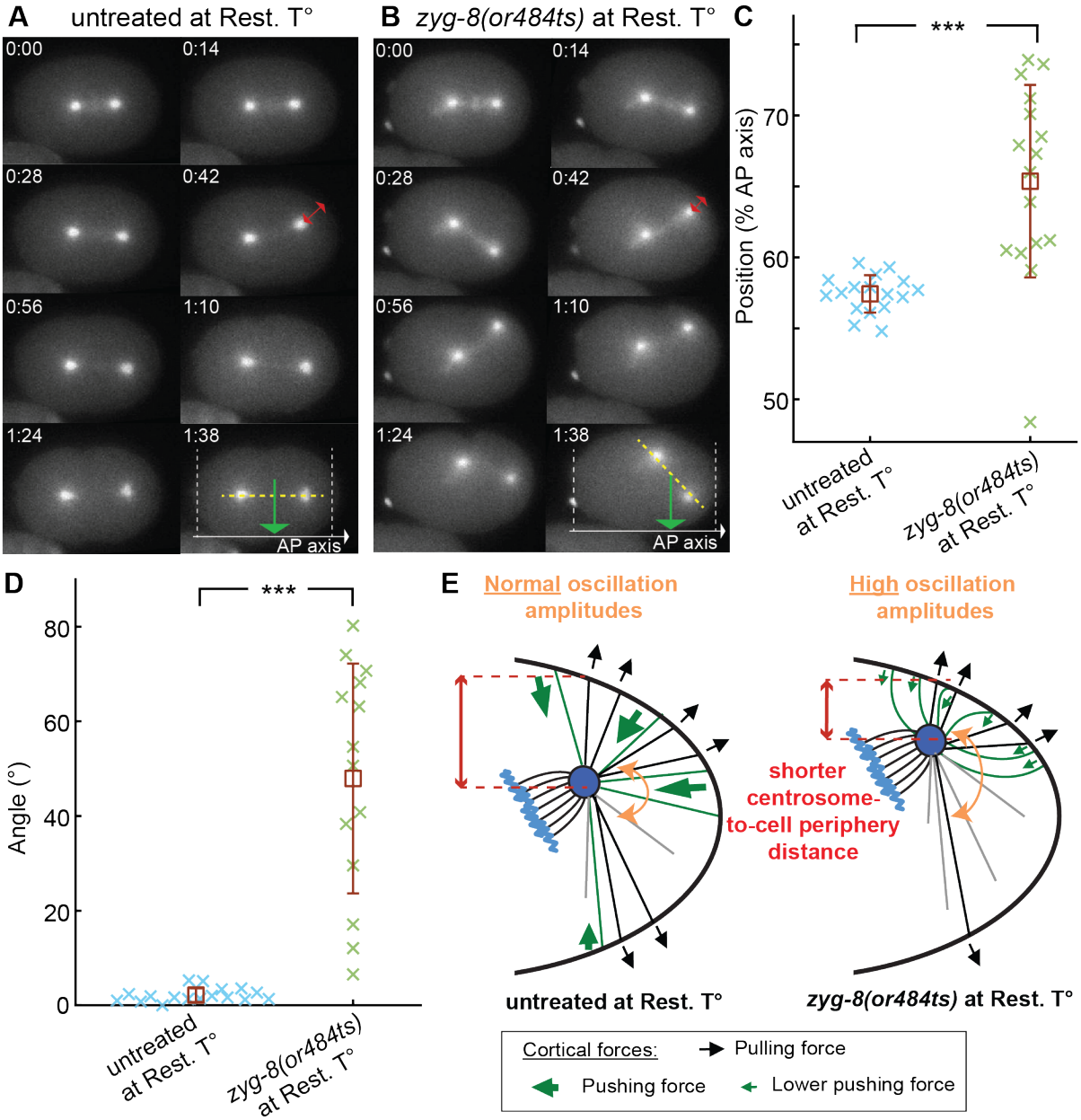


**Figure 8: In *zyg-8(or484ts)* mutants, overly soft microtubules result in a misoriented and mispositioned spindle at the anaphase end.**

(**A-B**) Time-lapse series of (A) an exemplar untreated embryo and (B) an exemplar *zyg-8(or484ts)* mutant along anaphase, both at the restrictive temperature (Rest. T°) and with EBP-2::mKate2 labelling. The green arrows indicate the spindle's final positions along the anteroposterior (AP) axis and the dotted yellow lines indicate the final orientations. The red double-headed arrows underline the minimal centrosome-to-cortex distances. The scale bars represent 10 µm. (**C-D**) Spindle final (C) positions along the AP axis and (D) angles for (light green) *N* = 14 *zyg-8(or484ts)* mutants and (light blue) *N* = 17 untreated embryos, both at the restrictive temperature. We tracked and analysed the centrosomes of embryos with EBP-2::mKate2 labelling (Method M7). The brown squares and error bars correspond to the means and SD. *** indicate significant differences with $p \leq 1x10^{-4}$ (Method M14). (**E**) Schematics illustrating how a large reduction in microtubule flexural rigidity, which reduces cortical pushing force, permits centrosome proximity to the cell cortex. This, in turn, causes defects in spindle positioning and orientation at the end of anaphase.

and the most-posterior position was also shifted closer to the cell centre (Figure S11A). Strikingly, depleting GPR-1/2 in *zyg-8(or484ts)* mutants rescued the spindle misorientation defects (Figure S11B). This finding indicated that low microtubule rigidity did not affect final spindle orientation when cortical pulling forces were reduced. These results highlighted the critical importance of maintaining a proper balance between cortical pulling and pushing forces for accurate spindle positioning and successful cell division.

In conclusion, sufficiently rigid microtubules were required to generate the centring force necessary during anaphase, when cortical pulling forces are at their peak. This centring force prevented the centrosome from being displaced too far from the centre, ensuring proper final orientation of the spindle (Figure 8E). Reliable spindle positioning at the end of mitosis is crucial for accurate cleavage furrow placement during cytokinesis, a process that determines the proper partitioning of cell fate determinants [106].

## DISCUSSION

Our work highlights a dual role for ZYG-8$^{DCLK1}$ during mitosis, involving the control of both microtubule rigidity and dynamics. This conclusion is based on three distinct, complementary genetic perturbations of *zyg-8*. We confirmed previous findings by Srayko *et al.*, showing that ZYG-8 modestly promotes microtubule growth while limiting the nucleation of astral microtubules in *C. elegans* zygote [42] (Figures 2 and 3). Importantly, we propose that ZYG-8 plays a major role in *C. elegans* spindle choreography, primarily by rigidifying the microtubules. Indeed, the modest changes observed in astral microtubule dynamics in the cytoplasm upon targeting *zyg-8*, as well as its potential role in stabilising microtubules, are insufficient to explain the phenotypes related to spindle pole oscillations during anaphase or the altered behaviour of astral microtubule contacts at the cell cortex. This proposition is supported by multiple lines of evidence. If ZYG-8's main function were to stabilise microtubules by reducing their catastrophe rate at the cell cortex, *zyg-8(RNAi)* treatment would be expected to decrease the cortical lifetimes of astral microtubules, similar to what was observed with *cls-2(RNAi)*, where both cortical pulling and pushing event lifetimes were reduced [71]. In contrast, we found that *zyg-8(RNAi)* increases the lifetimes of cortical pushing events (Figure 7B, D). This result also suggests that the main mechanism of action of ZYG-8 is not in preventing microtubule depolymerisation. Indeed, upon *klp-7(RNAi)*, which reduces microtubule depolymerisation, we previously observed a specific increase in pulling event lifetimes [71]. Similarly, if ZYG-8 primarily promoted microtubule growth, z*yg-8(RNAi)* should result in fewer astral microtubules reaching the cortex and shorter contact durations, as previously seen with *zyg-9(RNAi)* [71]. Instead, in our current study, we observed the opposite phenotypes (Figure 4C, E-F). Furthermore, if ZYG-8 limited microtubule catastrophe within the cytoplasm, then *zyg-8(RNAi)* would be expected to decrease the number of astral microtubule contacts at the cell cortex, as more microtubules would depolymerise before reaching it. This, again, contradicts our observations (Figure 4E). By contrast, the increased number of astral microtubule contacts upon *zyg-8(RNAi)* aligns with a role for ZYG-8 in limiting microtubule nucleation. However, this effect alone, which is moderate compared to nucleation perturbation upon targeting *spd-2*, cannot fully account for the observed variations in microtubule cortical-contact number. We propose that ZYG-8 also regulates microtubule rigidity, and that this function is the strongest contribution to the phenotype. Three independent experiments support this. First, less rigid microtubules bend more when growing against the cortex, reducing pushing force, delaying catastrophe onset, and increasing cortical

contact lifetimes (Figure 7A, D). Second, the altered frequency of spindle pole oscillations upon targeting *zyg-8* is consistent with a role in controlling microtubule rigidity [57, 68] (Figure 1D). Third, changes in microtubule shape in *zyg-8(RNAi)*-treated embryos and in *zyg-8(or484ts)* mutants further support this idea (Figures 5 and 6). Why ZYG-8 plays a greater role in regulating microtubule rigidity rather than microtubule dynamics. This is likely because ZYG-8 and EB compete for the same microtubule binding site at the corner of four tubulin dimers [36, 107, 108]. However, EB binds preferentially to the GTP cap at growing ends [107], while Doublecortin-family proteins bind *in vitro* to the whole lattice [109]. *In vivo*, DCX was excluded from microtubule ends [110]. An exclusion of ZYG-8 from microtubule ends in *C. elegans* zygote could account for differences in the efficiency of its dual role in regulating microtubule dynamics and rigidity. This may be particularly relevant in specific cellular contexts where proteins essential for microtubule growth or nucleation (e.g., γ-tubulin ring complexes) are absent or present at low levels. In neurons, proteins from the Doublecortin family are highly expressed and regulate microtubule rigidity [34, 92]. These proteins may also contribute to microtubule nucleation and/or growth, consistent with their *in vitro* capabilities [35, 82, 83, 113]. For instance, collateral branching in hippocampal neurons was significantly delayed following DCX depletion, possibly reflecting impaired microtubule dynamics [114]. Overall, ZYG-8$^{DCLK1}$ performs multiple microtubule-related functions in a context-dependent manner. We propose that the control of microtubule flexural rigidity represents a novel function during cell division and possibly beyond.

Looking ahead, it will be important to explore the mechanisms by which ZYG-8 rigidifies the microtubules. Several mechanisms have been proposed, primarily in the context of neurons. Here, we draw on the body of research on the DCX protein, which shares the same two microtubule-binding domains as DCLK1$^{ZYG-8}$. Besides, these two doublecortin domains are highly conserved in ZYG-8 [48]. (1) Microtubules can be rigidified by hindering the sliding of protofilaments through the binding of MAPs across these protofilaments. DCX binding on the microtubules is compatible with this mechanism since it reinforces lateral and longitudinal dimer couplings [35]. (2) Rigidification can also occur by bundling multiple microtubules together. Previous studies revealed such a mechanism for the Doublecortin family *in vitro* and *in vivo* [51, 81, 82, 92, 113, 115, 116]. In particular, *zyg-8(or484ts)* mutants displayed a perturbed bundle organisation of microtubules in touch receptor neurons [92]. However, in the *C. elegans* zygote, electron microscopy failed to reveal microtubule bundles in the spindle or astral microtubules close to the poles [117]. Therefore, we disfavour such a mechanism. (3) Microtubule rigidity is also regulated through post-translational modifications (PTM) [118-122]. Notably, a study showed that DCX expression increases tubulin polyglutamylation in neurons [123]. However, the *ttll-4(-);ttll-5(-);ttll-11(-)* triple mutants, which prevented tubulin glutamylation, did not show any defect in embryonic viability. It suggests that microtubule glutamylation may not significantly affect the zygote cell division [124]. (4) It was previously shown that damages along microtubule lattice soften microtubules [125, 126]. Thus, self-repair of local damages may also help restore the rigidity or stabilise the curved region [127]. Interestingly, the number of microtubule defects could notably correlate with the microtubule growth rate [128, 129]. The latter is particularly high in nematodes [130]. If a high occurrence of holes exists in the *C. elegans* embryo, ZYG-8 could contribute to healing as the Doublecortin family also acts as tubulin oligomer chaperones [83]. However, to date, there has been no evidence of microtubule lattice defects in *C. elegans* zygote. For example, embryos with EBP-2 fluorescent labelling did not show stationary fluorescent spots along the astral microtubules [42, 58]. The various mechanisms proposed above, in which ZYG-8 could play a key role in

regulating microtubule flexural rigidity, are not mutually exclusive; several of them may be combined. ZYG-8 rigidifying the microtubule by coupling the protofilaments appears to us the most plausible mechanism currently.

Focussing on mitotic spindle positioning in the *C. elegans* zygote, the current study both complements and departs from previous investigations**.** Firstly, we show that controlling microtubule flexural rigidity participates in the spindle choreography. In particular, this control helps prevent the spindle poles from approaching the cell periphery too closely during anaphase (Figure 8A, B, E). Consistently, we observe increased amplitudes of spindle pole oscillations following ZYG-8 or PTL-1 depletion (Figures 1C & S10A). This control through microtubule rigidity is complementary to the well-established regulation involving microtubule dynamics [25, 58, 63, 71]. Secondly, our study underlines that cortical pushing force contributes to spindle positioning during anaphase, although in a manner distinct from that of cortical pulling forces. Cortical pulling forces are dominant, and their asymmetry, controlled by PAR polarity, ensures spindle posterior displacement [65, 69, 90, 131-133]. To date, cortical pushing forces have been proposed to contribute to spindle centring during metaphase [25, 27]. During anaphase, although restoring forces are known to be necessary for spindle oscillations, the role of cortical pushing force as a restoring force was not demonstrated [57]. Besides, it is often assumed that cortical pushing force plays a minimal role during anaphase, due to the high magnitude of cortical pulling forces and the dampening effect of microtubule buckling [59, 70, 134]. However, we report that weakening the cortical pushing forces, as observed in *zyg-8(or484ts)* mutants, hinders spindle alignment along the AP axis (Figure 8B). This force imbalance compromises the final position and orientation of the spindle (Figure 8C-D). Interestingly, decreasing cortical pulling force by depleting GPR-1/2 in *zyg-8(or484ts)* mutants rescues the spindle misorientation phenotype (Figure S11). Together, these findings highlight the importance of sufficiently strong cortical pushing forces during anaphase, which contribute to proper force balance and ensure accurate spindle orientation at the end of mitosis. Thirdly, we show that in *zyg-8(or484ts)* mutants, astral microtubules are still able to contact the opposite cortex (Figure 5A, Movies S5 and S6). This rules out a model in which spindle misorientation arises from a failure of microtubules to reach the cortex, as previously suggested [48]. Overall, the astral microtubule network functions like a spring, restricting the spindle transverse motion away from the centre in *C. elegans* zygotes [25, 27, 68]. From this perspective, microtubule flexural rigidity emerges as a key physical parameter controlling the magnitude of centring forces. This mechanical contribution is essential for generating cortical pushing forces strong enough to counteract the intense cortical pulling forces that act during anaphase.

We foresee that the essential role for pushing extends beyond the nematode's first division and may be relevant to other asymmetric divisions and maybe further. It is well established that the pulling forces dominate spindle orientation. It is accounted for by the canonical model based on the molecular machinery composed of the cortical G$\alpha$-LGN$^{GPR}$-NuMA$^{LIN-5}$ complex and the cytoplasmic dynein motor [10, 135]. However, less attention has been paid to the contribution of the pushing forces to spindle orientation [136]. The dependence of spindle orientation on cell shape, which is often neglected, suggests that the pushing force could play a significant role in this process [137-141]. In other systems, some studies found that the spindle did not align with the dynein-enriched cortical zones [142-145]. Consequently, the traditional canonical model alone cannot account for spindle orientation in various contexts. We propose that the cortical pushing force contributes to this phenomenon and that the

flexural rigidity of microtubules must be sufficiently high. Notably, the orientation of the mitotic spindle defines the direction in which a cell divides. Therefore, many biological processes, ranging from germline stem cell division to epithelial tissue homeostasis and regeneration, require correct mitotic spindle orientation. Defects in spindle orientation have been associated with various diseases, such as organogenesis and morphogenesis failures, or cancer [146-153].

By uncovering ZYG-8's dual role in *C. elegans* mitosis, we can now question its contribution to zygote meiosis, especially through controlling microtubule flexural rigidity. A recent study highlighted that ZYG-8 promotes meiotic spindle stability and suggested that it may regulate microtubule dynamics and motor-driven forces [50]. We wonder whether some of the perturbations that they observed upon targeting *zyg-8* could be attributed to the deregulation of microtubule rigidity. Notably, they found that most *zyg-8(or484ts)* meiotic spindles were significantly bent at the restrictive temperature. Additionally, some images of the mutant showed microtubules exhibiting high local curvatures. Similar perturbations were also observed following ZYG-8 depletion using the Auxin-inducible degradation system. In light of these observations, it is plausible that ZYG-8 contributes to the assembly or/and stability of meiotic spindles in the zygote by stiffening microtubules.

In conclusion, our findings regarding the pivotal role of ZYG-8$^{DCLK1}$ in spindle positioning and orientation, primarily through rigidifying microtubules during mitosis, offer not only a deeper understanding of the fundamental mechanisms governing cell division but also highlight significant implications for cancer therapy. Given that DCLK1 is frequently deregulated in various solid tumours (e.g., those from the colon, pancreas, kidney and breast), this suggests its involvement in a common process such as cell division [154-157]. Additionally, as the proteins of the Tau family are also found to be deregulated or mutated in cancers, targeting microtubule rigidity may represent a promising approach for future cancer treatments [158-160]. This strategy could potentialise existing therapies targeting microtubule dynamics, which often suffer from side effects and are limited by cancer cell resistance.

## MATERIAL AND METHODS

### *M1- C. elegans strains and their culturing*

The *C. elegans* strains used in the present study are listed in Table S1. *C. elegans* nematodes were cultured as described in [161] and dissected to obtain embryos. The strains were maintained at 20°C, except the thermosensitive mutant *zyg-8(or484ts)* maintained at 15°C and AZ244 maintained at 25°C to increase transgene expression. The strains were handled on nematode growth medium (NGM) plates and fed with OP50 *E. coli* bacteria.

### *M2- RNAi feeding*

RNA interference (RNAi) experiments were performed by feeding, as described in [162]. Bacteria were obtained by Source BioScience (*zyg-8*: III-6C10; *ptl-1*: III-1A12; *spd-2*: I-4O08; *zyg-9*: II-6M11; *cls-2*: III-4J10; *klp-7*: III-5B24; *gpr-1/2*: III-4J09). The feedings were performed at 20°C, except for *gpr-1/2* realised at 15°C to be at the restrictive temperature of *zyg-8(or484ts)* mutant. For RNAi targeting of *gpr-1/2, zyg-8* and *ptl-1*, the treatment lasted 96 hours and dsRNA expression was induced with 4 mM of IPTG (Isopropyl β-D-1-thiogalactopyranoside). For *spd-2*, *zyg-9*, *klp-7* and *cls-2*, dsRNA expression was induced with 3 mM IPTG. The RNAi treatment duration was 6 hours for *zyg-9* and *spd-2*, 24 hours for *klp-7*, and 48 hours for *cls-2*. The control embryos for the RNAi experiments were fed with bacteria carrying the empty plasmid L4440.

### *M3- Preparation of the embryos for live imaging or immunofluorescence*

For live imaging, embryos were dissected in M9 buffer (prepared by combining 3 g $KH_2PO_4$, 6 g $Na_2HPO4$, 5 g NaCl and 1 mL of 1 M $MgSO_4$ diluted in ultrapure water to 1 L) and mounted on a pad (2% w/v agarose, 0.6% w/v NaCl, 4% w/v sucrose) between a slide and a coverslip.
For immunofluorescence staining, embryos were dissected in M9 buffer and mounted on a slide coated with poly-L-lysine (0.1%) (Sigma-Aldrich P1524). The slides were dipped in liquid nitrogen to crack the embryo's eggshell and immediately transferred to -20°C methanol for fixation for 20 minutes (freeze-cracking method [163]). They were then rinsed for 10 minutes in PBS 1X before blocking for 20 minutes in PBS-Tween (0.2%) with BSA (1%).
Importantly, for the thermosensitive *zyg-8(or484ts)* mutants, we transferred them as L4 larvae to 25°C and incubated for 15 hours before use, as previously done in [48].

### *M4- Fluorescence microscopic imaging conditions*

The various microscopy setups used are presented in the table below. Embryos were imaged at 23°C, except otherwise stated. Images were stored using the Omero software [164].

| Imaging experiment | **Spindle pole imaging** | **(1) Landing assay to study microtubule cortical contacts; (2) Microtubule dynamics (growth and nucleation rates)** | **(3) Microtubule network; (4) ZYG-8 localisation inside the embryo** | **(5) Microtubule live imaging** |
|---|---|---|---|---|
| Live or fixed embryo | Live | Live | (3) & (4): Fixed | Live |
| Microscope type | Zeiss Axio Imager upright | Leica DMi8 equipped with CSU-X1 spinning disk head (Yokogawa) | (3) & (4): Airyscan 2 Zeiss LSM980. | Nikon AX |

| | | | | |
|---|---|---|---|---|
| Fluorescent labelling | Spindle poles, e.g. mCherry::TBG-1 | (1) Microtubules: GFP::TBB-2 or mCherry::tubulin.<br>(2) Microtubule plus-ends : EBP-2::mKate2 | (3) DM1A-AF488 conjugate.<br>(4) mNG::ZYG-8 and mCherry:tubulin. | GFP::TBB-2 |
| Objective | 100x/1.45 NA Oil plan-Apo | 100x/1.4 NA Oil HCX Plan Apo | 63x/1.4 NA Oil Apochromat DIC M27 | 63x/1.42 Oil Plan Apo OFN25 DIC N2 |
| Acquisition plane(s) | Spindle plane | (1) Cortex plane close to the glass slide (located 12-15 µm below the spindle plane).<br>(2) For *zyg-8(RNAi)*: spindle plane; for *zyg-8* overexp. and *zyg-8(or484ts)*: ~3 µm below spindle plane | (3) 25-30 or (4) 10-12 z-sections centred at the spindle plane;<br>z-step: (3) 0.17 µm, (4) 0.3 µm. | Spindle plane |
| Camera / detector | Andor iXon3 EMCCD 512x512 | ultra-sensitive Roper Evolve EMCCD | Airyscan detector | Nikon NSPARC detector |
| Illumination, excitation and emission characteristics | Illumination: mercury lamp.<br>NG channel: excitation: enhanced transmission (ET) 485/12 bandpass (BP) (AHF analysentechnik); beamsplitter: low pass (LP) 495; emission: 525/50 ET Bandpass<br>mCherry channel: excitation: BP 530-585; beamsplitter: 600; emission: low pass 615 | Illumination: Argon laser<br>mCherry channel: laser selecting the line at 561 nm with DAPI-GFP-mCherry-Cy5 emission filter and a Quad Dichroic filter.<br>GFP channel: laser selecting the line at 488 nm with GFP/FITC 4 nm BP excitation filter and retrieving fluorescence with a Quad Dichroic emission filter | Illumination: laser diodes<br>(3) excitation wavelength 488 nm; main beam splitter (MBS) 488/639 and 405.<br>(4) excitation wavelength 488 nm or 561 nm; MBS 488/561 and 405;<br>secondary beam splitter LP525 (for 488 nm laser) or SP550 (for 561 nm laser). | Illumination: laser excitation wavelength 488 nm; Emission filter 502-546 nm. |
| Spatial resolution (µm/pixel) | 0.16 | 0.14 | (3) & (4): 0.04. | 0.115 |
| Temporal resolution | 32.498 frame/s | (1) 10 frame/s<br>(2) 2.5 frame/s | (3) 41.6 s per frame<br>(4) 1 min 23 s per frame | 1.962 s per frame |
| Additional parameters or equipment | Extra anti-heat and ultraviolet filters added to the mercury lamp light path for long-term time-lapse | Adaptive Focus Control (AFC, Leica) | Mode: (3) & (4): Super Resolution.<br>Averaging: (3): line, number: 2 lines, method: mean; (4) none. | Mode: Galvano unidirectional; Super resolution<br><br>Integrating: 2<br>Dwell time: 2 µs |
| Post-processing | None | None | Deconvolution | None |

| | | | | |
|---|---|---|---|---|
| Software | Andor Solis (Oxford instruments) | Imaging Solution (Inscoper, SAS) | ZEN blue (Zeiss) | NIS-Elements AR |

***M5- Localisation of ZYG-8 in the C. elegans one-cell embryo***

To study ZYG-8 localisation in the zygote, we used *C. elegans* strains expressing fluorescently labelled microtubules (mCherry::tubulin) and fluorescently labelled ZYG-8 (mNG::ZYG-8) (Figures S1A-C and S1G-I). We analysed deconvolved dual-colour images of fixed embryos acquired using the Zeiss Airyscan 2 microscope. First, we computed the intensity profiles of both mCherry::tubulin and mNG::ZYG-8 signals along a 5-pixel wide line (Figures S1D-E, J-K). The lines used for this analysis are shown in Figure S1D, J. Co-localisation of intensity peaks indicated the binding of ZYG-8 to microtubules. Second, we investigated pixel-wise co-localisation by producing a scatterplot and computed Pearson's correlation coefficient *r* (Figure S1F, L). Statistical significance was assessed through the Costes statistical test using 200 rounds of randomisation and a bin width of 0.001 [165]. These analyses were performed using Fiji and the JACoP plugin [166]. To test ZYG-8 localisation specifically on astral microtubules, we computed the Pearson's coefficient after masking the spindle area in the images.

***M6- Quantification of ZYG-8 level at the worm and embryo scales***

To quantify the ZYG-8 level at the worm scale, we performed a Western blot analysis using protein extracts obtained from different *C. elegans* strains (Figure S2A-B). For each experiment, 30 adult hermaphrodites were picked into 200 µL of M9 buffer and snap-frozen in liquid nitrogen, then thawed, mixed with 6.5 µL loading buffer (DTT 0.1 M), and loaded onto a Mini Protean TGX 4–20% Tris-Glicine gel from Bio-Rad (Hercules, CA). Immunoblots were probed using the primary anti-OLLAS antibody (Novus Biologicals NBP1-06713, 1 mg/mL, host: rat) diluted at 1/2000 and the primary anti-tubulin antibody (Sigma-Aldrich T5168, host: mouse) diluted at 1/2000, and then revealed using an HRP (horseradish peroxidase) conjugated secondary antibody (1:20000; Jackson ImmunoResearch, West Grove, PA; host: rat for antiOLLAS & mouse for anti-tubulin). Membrane saturation and all antibody dilutions were made in PBS–Tween 0.2% and 5% non-fat dry milk. Blots were incubated with WesternBright ECL spray (Advansta K-12049-D50) before detecting by chemiluminescence on an Amersham Imager 680 (GeHealthcare, Chicago, IL). Quantification was performed using Fiji [167].

To complement the first quantification, we analysed deconvolved dual-colour images of embryos carrying two fluorescent tags: mCherry::tubulin and mNG::ZYG-8. For each embryo, we realised, in the same regions of interest (ROI), red and green fluorescence intensity measurements (mean within ROIs) using Fiji: 2 square ROIs (40 x 40 pixels; 1.6 x 1.6 µm) within the spindle (1 per half-spindle), 3 square ROIs (40 x 40 pixels) within the cytoplasm, 5 curvilinear ROIs on astral microtubules using the segmented line tool, and a ROI (40 x 40 pixels) outside the embryo, the latter to measure the background fluorescence. Exemplar ROIs are highlighted in Figure S2C. For spindle and cytoplasm measurements, fluorescence quantification was performed on maximum projected images (3 z-sections centred on the spindle mid-plane). After subtracting the background fluorescence (mean intensity in corresponding ROI) from each fluorescence of interest (spindle, cytoplasm and astral microtubule) and for each channel separately, we computed the ratio of ZYG-8 fluorescence over tubulin fluorescence for the three measurements (Figure S2G, H).

***M7 - Centrosome-tracking assay and oscillation characterisation***

The tracking of labelled centrosomes (e.g., mCherry::TBG-1) and the analysis of their trajectories were conducted using custom tracking software developed using Matlab (The MathWorks) [57]. Tracking of γ-tubulin labelled embryos fixed in -20°C methanol demonstrated an accuracy of 10 nm [25]. To determine embryo orientations and centres, we performed cross-correlation of the embryo background cytoplasmic fluorescence with artificial binary images that represented an embryo. We calculated the embryo size (lengths of the long and short axes) using the active contour algorithm [168]. From the spindle pole positions, we measured the maximal amplitudes of anaphase oscillations (peak-to-peak) for both poles, normalised to the length of embryo's short axis, as well as the frequencies of these maximal oscillations (e.g., Figures 1 and S3). We also assessed mitotic spindle length, normalised to the length of embryo's long axis, and the maximal spindle elongation rate following nuclear envelope breakdown (e.g., Figure S6D). Finally, we quantified the spindle position (the midpoint between the two centrosomes), and the spindle orientation (the angle between the spindle axis and the embryo's long axis) at the end of mitosis, specifically at 150 s after the anaphase onset (e.g., Figure 8C-D).

***M8 - Characterisation of astral microtubule growing and nucleation rates***

We labelled microtubule plus-ends using EBP-2::mKate2, which form comet-like structures as the microtubules grow (Figures 2A and 3A). We performed an analysis of the comets adapted from the article by Srayko *et al.* using Fiji (except otherwise cited) [42]. We measured microtubule dynamics during metaphase.

To measure the growth rates, we first denoised the movies using Kalman filtering, with the gain set to 0.5 and the initial noise estimate set to 0.05 [169] (Figure 2A). Next, we traced a line along the comet trajectory in the pre-processed movie, restricting to comets that remained visible for at least 10 frames (4 s). We generated a kymograph from the traced line to assess comet displacement velocity. We repeated the measurement approximately 50 times for each condition across about ten embryos (about 25 comets per centrosome).

To measure the nucleation rate, we first denoised the movies using Candle filtering (parameters: *beta* = 0.1; *patchRadius* = 1; *searchRadius* = 3; *back* = 1) (Figure 3A). We did not apply additional pre-processing for *zyg-8(RNAi)* treatment, *zyg-8* overexpression and their control. However, for *zyg-8(or484ts)* mutants and untreated embryos, we enhanced contrast using an unsharp mask (*radius* = 1; *Mask weight* = 0.7). Since centrosomes moved during metaphase, we applied Icy's rigid registration plugin (v1.4) on the denoised images [170]. This registration aligns each image with a reference image to correct for centrosome displacements, as described in [171]. Doing so, we accurately counted the comets crossing a half-circle region of interest (ROI) positioned 9 μm from the centrosome after [42]. We generated kymographs over 150 frames (60 seconds). To address the inhomogeneous background in the raw kymographs, we applied background subtraction using Gaussian blurring. We then set an intensity threshold to retain the brightest 2% of pixels in *zyg-8(RNAi)* and control kymographs, and 2.5% for *zyg-8* overexpression ones, *zyg-8(or484ts)*, and their controls. Finally, we used the "Analyse particles" command and counted objects considered as individual EBP-2 comets (particle size: 2 pixels to infinity, 0.14 μm/pixel). Measurements were done for both anterior and posterior centrosomes, except when only a single centrosome was clearly visible.

***M9 - Centrosome-size measurements***

We analysed images of embryos labelled with either mCherry::TBG-1 and mCherry::HIS-58, or GFP::TBG-1 and GFP::HIS-11, by tracking their centrosomes (cf. M7). Based on the tracked positions, we extracted vignettes of 6.4 x 6.4 µm (40 x 40 pixels; Figure 3E, F). We then performed a 2D Gaussian least-square fit to characterise both the posterior and anterior centrosomes every second [172]. From these fits, we obtained the *x*- and *y*-widths and calculated the diameter of the centrosomes, assuming they are round, using the formula: $D = \sqrt{x^2 + y^2}$.

***M10 - Landing assay to study astral microtubule cortical contacts***

The entire microtubule lattices were fluorescently labelled using GFP::TBB-2 or mCherry::tubulin to view them in all their states. We used the same approach as the one previously implemented in [71] and available on Zenodo (doi: 10.5281/zenodo.4552485); we combined a Kalman filtering [169] (gain set to 0.5 and initial noise to 0.05) and *u-track* [173] whose parameters are listed in the table below. Movies S1–S4 show representative examples of microtubule contact tracking under the four conditions we studied. After tracking the microtubule contacts, we quantified the number of microtubule cortical contacts per frame, averaged the values over a 10-second window, and normalised them by the embryo area. This provided an instantaneous count of microtubule contacts throughout mitosis for each embryo, which we then averaged across embryos within each experimental condition (e.g., Figure 4C). We also computed the duration histograms of astral microtubule contacts per embryo and averaged these histograms across embryos for each condition (e.g., Figure 4E).

We then performed the DiLiPop analysis. This statistical analysis of the microtubule cortical contact durations reveals the short-lived and long-lived populations of astral microtubules at the cortex associated with pulling and pushing events, respectively [71]. By globally fitting the embryo-set duration distributions of a given condition, we obtained the characteristic lifetimes and densities of the cortical pulling and pushing events (e.g., Figure 7B-E). Error bars of the lifetimes and densities were obtained by bootstrapping as explained in [71]. These densities of events are distinct from instantaneous contact density and thus independent of the cortical contact durations (except in the case of anaphase pulling events due to all force generators being involved in pulling). We noticed that the lifetimes of pulling and pushing events in the present study differed from those in our previous work [71]. This discrepancy likely stemmed from differences in microtubule labelling (GFP::TBB-2 vs. YFP::TBA-2) and variations in microscope sensitivity. Therefore, we consistently compared results from experiments conducted within the same time frame (within two months).

| **u-track step** | **Parameter name** | **Parameter value** |
|---|---|---|
| Detection | Gaussian standard deviation | 1.2 |
| | Alpha-value for initial detection of local maxima | 0.14* / 0.12** |
| | Rolling window time-averaging | 3 |
| | Iterative Gaussian mixture-model fitting | 0 |
| Tracking | Maximum gap to close | 5 |
| | Merge split | 0 |
| | Minimum length of track segments from the first step | 1 |
| Cost function frame-to-frame linking | Flag for linear motion | 1 |
| | Allow instantaneous direction reversal | 1 |
| | Search radius lower limit | 1 |
| | Search radius upper limit | 3 |

| | | |
|---|---|---|
| | Standard deviation multiplication factor | 3 |
| | Nearest neighbour distance calculation | 1 |
| | Number of frames for nearest neighbour distance calculation | 4 |
| Cost function close gaps | Flag for linear motion | 1 |
| | Search radius lower limit | 1 |
| | Search radius upper limit | 3 |
| | Standard deviation multiplication factor | 3 |
| Nearest neighbour distance calculation | Number of frames for nearest neighbour | 4 |
| | Penalty for increasing gap length | 1.5 |
| | Maximum angle between linear tracks segments | 30 |

* for GFP::TBB-2 labelling; ** for mCherry::tubulin labelling.

***M11 - Mapping astral microtubules and characterising their local curvatures and their tortuosity***

We stained microtubules using an anti-α-tubulin antibody, clone DM1A raised in mouse, Alexa Fluor® 488 conjugate (Sigma-Aldrich 16-232), diluted at 1/500 in PBS-Tween (0.2%) with BSA (1%). It targets several α-tubulin isoforms in various species. Antibody incubation was performed overnight at 4°C. Slides were then rinsed for 10 minutes in PBS-Tween (0.2%), twice, in a light-free environment. We could then visualise microtubules all along their length. We identified the z-section(s) as the more appropriate for astral microtubule segmentation. For most embryos, we found a single z-section per embryo for which both centrosome asters were visible. For some embryos having the two centrosomes on distinct z-sections, we considered two planes of interest.

Five-step image processing pipeline to map the local curvatures of the astral microtubules (Figure S8A). **(1)** We used the planes above and below the plane of interest to perform an extended depth of field projecting the 3 z-sections into a single image (Figure S8B) [174]. We thus better visualise microtubules all along their length. **(2)** We applied the *Orientation Filter Transform* (OFT, number of orientations = 20; radius = 5 pixels) since it is effective in enhancing filamentous pattern against noises [20, 175] (Figure S8C). **(3)** We then used the interactive machine-learning tool, *Ilastik,* to segment the astral microtubules (Figure S8D). The dedicated paragraph below provides more detailed information about our segmentation. **(4)** We generated the skeleton of the filament traces from the binary segmentation, taking advantage of *SOAX* (Figure S8E). Further information about the use of SOAX is available in a dedicated paragraph below. **(5)** We finally measured the local curvatures of astral microtubules pixel-by-pixel from the skeleton coordinates, enabling mapping of the local curvatures (Figure S8F). For a set of three neighbouring points sampling the curve, the local curvature corresponds to the inverse of the radius of the circle going through the mid-point and best fitting the two others. Local curvatures were computed along microtubules according to the three-point method [176] using a code retrieved on Matlab Central [177]. In a nutshell, microtubules are viewed as parametrised curves; at each point, the *x* and *y* coordinates are represented as second-order polynomials of the curvilinear abscissa passing through the point and its two neighbours. The curvature is then computed with the Frenet-Serret formula.

*Ilastik*: We initially trained *Ilastik* using the conditions *zyg-8(RNAi)* and its control RNAi during metaphase. This involved approximately 10 manual annotations of microtubules across three embryos for each condition to cover various intensities, contrasts and microtubule shapes.

We then used this trained model, referred to as #1M (M for metaphase), to segment, in a semi-supervised way, the astral microtubules in metaphase images. Next, we trained the model to segment anaphase images of *zyg-8(RNAi)*-treated embryos and their controls. Indeed, denser microtubule networks in anaphase required additional annotations. This led to the upgraded model #1A that we used to segment anaphase images. We then analysed *zyg-8(or484ts)* mutants and untreated embryos in metaphase. The model was further improved by manually annotating three mutants, resulting in model #2M, which we used to segment images of both mutants and untreated embryos in metaphase. We applied a similar process for segmenting anaphase images of mutants and untreated embryos, enhancing model #2M with a few annotations of anaphase mutants to get the model #2A. The table below summarised the *Ilastik* models used to produce the data displayed in the different figures.

| ***Ilastik* model** | **Used for data displayed in figures** |
|---|---|
| #1M | 6A; 6E & 6G (only *zyg-8(RNAi)* and its control RNAi) |
| #1A | 6B; 6F & 6H (only *zyg-8(RNAi)* and its control RNAi) |
| #2M | 6C; 6E & 6G (only *zyg-8* mutant and untreated embryo at Rest. T°) |
| #2A | 6D; 6F & 6H (only *zyg-8* mutant and untreated embryo at Rest. T°) |

*SOAX*: We extracted the centrelines from the thick filaments utilising SOAX mostly with standard parameters. We made the few specific adjustments highlighted in the table below. These five adjusted parameters were crucial for accurately delineating the curved regions of the microtubules. The settings used ensured that the centrelines faithfully represented the shapes of the microtubules, as confirmed through visual validation. Additionally, manual corrections could be applied at this stage, especially when two microtubules were mistakenly merged into one.

| ***SOAX* parameter name** | **Parameter value** |
|---|---|
| Snake Point Spacing | 4 |
| Beta | 0.01 |
| Stretch Factor (k_str) | 0.8 |
| Radial Near (pixels) | 8 |
| Radial Far (pixels) | 16 |

Microtubule shape quantification: We analysed only the astral microtubules that were at least 4 μm long after segmentation, as shorter ones often represented fragments. This approach was appropriate for comparing conditions without seeking absolute quantification. We conducted three complementary approaches.

(1) For each z-projected stack, we calculated the normalised histogram of local curvatures with a bin size of 0.05 $\mu m^{-1}$ (Figures S7A & S8G) and averaged these histograms per condition (Figure 6A-D). The curvatures, expressed in per micrometre, range from 0.025 to 1 $\mu m^{-1}$, corresponding to curvature radii from 40 μm to 1 μm, respectively. 40 μm could be interpreted as mostly straight astral microtubules.

(2) We computed the 95$^{th}$ percentile curvature for each microtubule to capture faithfully the highest curvatures (Figure S7B) and then calculated the median of these values across all microtubules in each z-projected stack. Each stack exhibited 15 to 74 microtubules. We finally compared the set of medians between two conditions (Figure 6E, F).

(3) We measured the tortuosity for each microtubule, defined as the curvilinear distance divided by the end-to-end distance (Figure S7C). Straight microtubules have tortuosity values

near one, while bent microtubules show higher values. Then, we calculated the medians of tortuosity values across all microtubules in each z-projected stack, and compared the set of medians between two conditions (Figure 5G, H).

***M12 - Simulation using Cytosim***

We used *Cytosim* to simulate cytoskeletal filaments [102]. We modified *Cytosim* to allow multiple fibre types to emanate from a single aster and to exert a given external force on solids, fibres or spheres (doi: 10.5281/zenodo.14246919). We conducted a 2D simulation of the first mitosis of the *C. elegans* zygote, focussing on spindle positioning and the astral microtubule network (Figure S9A). The simulation represented the spindle as a rigid rod implemented with static spindle microtubules, excluding any dynamic elements such as motor proteins. The parameters used in the simulation are detailed in Table S2 and the simulation files are provided as supplemental files S1, S2 and S3 with an exemplar video for each microtubule rigidity (Movies S8-S10). Importantly, to mimic cortical asymmetric pulling forces, we applied external forces at the spindle poles: -180 pN at the anterior pole and +300 pN at the posterior pole [69]. We used solids to simulate the centrosomes and attached two types of fibres to each, to differentiate between spindle and astral microtubules. The astral microtubules were defined as fibres without dynamics at their minus ends and with plus-ends displaying classic dynamic instability. We set their total number to 75, according to our estimated count of astral microtubules longer than about 2 µm in a 2D plane. Their rigidities were set to 2, 10, or 25 pN·µm², reflecting the range of *in vitro* measurements varying between 3.7 and 26 pN.µm$^2$ [21]. All microtubule dynamic parameters were kept constant across simulations. Additionally, these fibres could engage with cortical force generators simulated as hands bound to the cortex.

We measured both the highest curvatures (95$^{th}$ percentile) and the tortuosity of the astral microtubules (Figure S9B-C) after 45 seconds of simulation, following the approach outlined in method M11. To estimate the durations of fibre cortical contacts, we analysed fibre lengths, end positions, and cortical anchor positions. When microtubules push against the cortex, they grow slowly due to the force-velocity relationship, remaining near the cell cortex. We first recovered fibre lengths over time to identify instances of very low growth rates (under 0.18 µm/s), indicating moments when the fibres were stalled (neither growing nor shrinking). Next, we filtered out stalled fibre ends further than 1 µm from the cortex. We allowed 15 s for warming-up and considered cortical contacts during the next 45 s to compute the duration histogram. We then fitted it with a mono-exponential model [58, 178]. This analysis yielded a characteristic lifetime for each simulation (Figure S9D). We realised 40 simulations per condition.

***M13- Fourier analysis of the positional micromovements***

We investigated the micromovements of spindle position along the transverse axis over time, based on our previously published method [25]. From the time series of the spindle position along the transverse axis during anaphase obtained by tracking the poles (cf. M7), we computed the power spectral density (*PSD*) of the signal multiplied by the Hann window to safeguard against artefact due to the position difference between the beginning and end of the considered time interval [179]. It contrasted with [25], where we selected only embryos with low drift in their position over time, rather than windowing. The Hann windows appeared to be a sensible choice for fitting the *PSD* later since its discrete Fourier transform has only

three non-zero coefficients [179, 180]. Therefore, once convolved to the real *PSD* of the spindle length, it minimally "blurs" it.
We then fitted this *PSD* with a second-order Lorentzian model, as in [25]. Along a mechanistic line, this model corresponds to a Kelvin-Voigt-with-inertia discrete model corresponding to a Hookean spring (centring, *K*), a dashpot (damping, *G*), and an inertial element (*I*) in parallel. However, these quantities, when retrieved by fitting, depend on the amplitude of the stochastic noise that powers the fluctuations. We, therefore, utilised an alternative representation featuring (1) a diffusion coefficient *D*, inversely proportional to the damping *G* and dependent on the stochastic noise powering the fluctuations [25], (2) the centring-to-damping corner frequency $f_c$ ($\propto K/G$) reflecting centring efficiency, and (3) the damping-to-inertia corner frequency $f_0$ ($\propto G/I$); the inertia *I* arising from load-dependent detachment of force generators as for anaphase rocking [57]. Such a model was transformed into the Fourier space and convolved on the fly with the transform of the Hann window to perform the fit [179]. We then performed the fit using augmented Lagrangians and refined it using the pattern search algorithm [181, 182] as implemented in [179]. To quantify the variability from biological origin of the spectrum over *N* embryos, we estimated the confidence interval at significance 0.05 using bootstrap with bias-corrected and accelerated percentile method [183, 184]. In particular, it involved performing 30 iterations of fitting a set of *N* embryos drawn with replacement from the available ones. We filtered out 4/30 draws in the case of non-treated paired with *zyg-8* overexpression as the fit resulted in a too-low likelihood.

***M14- Statistics***
The difference between two samples was assessed by the two-tailed Student's *t*-test with Welch–Satterthwaite correction for unequal variance. When Gaussian distribution cannot be assumed, we used the Mann–Whitney test (also known as the Wilcoxon rank-sum test). We used it for instance to compare microtubule highest curvatures (e.g., Figure 6E) or microtubule tortuosity (e.g., Figure 6G). For the sake of simplicity, we reported confidence levels using diamond (◊, $0.01 < p \leq 0.05$), stars (*, $0.001 < p \leq 0.01$; **, $1x10^{-4} < p \leq 0.001$; ***, $p \leq 1x10^{-4}$) or ns (non-significant, $p > 0.05$). We abbreviated the standard deviation by SD. Last, we used the Kolmogorov–Smirnov test to reveal whether the two distributions differed significantly (distributions of contact durations or of local curvatures).

**Acknowledgements**

Some *Caenorhabditis elegans* strains were provided by the Caenorhabditis Genetics Center (CGC), which is funded by National Institutes of Health Office of Research Infrastructure Programs (P40 OD010440; University of Minnesota). Strains TH27 and TH30 were kindly offered by Prof Anthony A. Hyman. We thank Dr Grégoire Michaux for supplying the feeding clone library and for technical support. Strains MCP347, MCP361 & MCP554 were generated by SEGiCel (SFR Santé Lyon Est CNRS UAR 3453, Lyon, France) with the support of CNRS and IBiSA. We thank S. Dutertre and X. Pinson of the Microscopy Rennes Imaging Center (MRic, BIOSIT, Biogenouest) for their assistance. MRic is part of the national infrastructure France-BioImaging supported by the French National Research Agency (ANR-10-INBS-04). In particular, we acknowledge funding for the Zeiss Airyscan confocal microscope through EU FEDER (CARE Phase 2), the Zeiss Airyscan 2 confocal microscope via INCA, Rennes Métropole,

CPER and Biosit, and the Nikon Nsparc confocal microscope through grants from INSERM (G. Michaux), ANR (GroBluRe, G. Michaux), and AIS Rennes Métropole (H. Boukhatmi). The spinning disc microscope was co-funded by the CNRS, Rennes Metropole (AIS 16C0400, H. Bouvrais) and Region Bretagne (AniDyn-MT grant, J. Pécréaux). L.C. was supported by a PhD fellowship from “La Ligue Nationale Contre le Cancer” (2021-2024). H.B. was supported by the ANR grant MICENN, and by “La Ligue Régionale Contre le Cancer » (Ille-et-Vilaine & Deux-Sèvres committees, 2019 ; Côtes d’Armor & Ille-et-Vilaine committees, 2021), as well as the University of Rennes (Défis scientifiques, 2019). We thank the Pécréaux lab for their support, and the Gibeaux, Giet, Huet, Michaux, and Tramier labs for helpful discussions. We also thank L. Chesneau for assistance in designing the CRISPR strains, and A. Pacquelet, B. Lacroix and C. Heligon for their careful reading of the manuscript.

## Author contributions

Conceptualisation: HB, JP; Experimental data: LC, EH, LS, SP, MC, TS, HB; Data curation: HB; Formal analysis: LC, EH, MC, JP, HB; Funding acquisition: JP, HB; Methodology: LC, JP, HB; Project administration: HB; Software: JP, HB; Supervision: JP, HB; Validation: LC, EH, JP, HB; Visualisation: LC, HB; Writing – original draft: HB; Writing – review and editing: LC, JP, HB.

## Disclosure and competing interests statement

The authors declare that they have no conflict of interest.

**REFERENCES**


1. Matis M. The Mechanical Role of Microtubules in Tissue Remodeling. BioEssays. 2020;42(5):1900244. doi: https://doi.org/10.1002/bies.201900244.
2. Rizzelli F, Malabarba MG, Sigismund S, Mapelli M. The crosstalk between microtubules, actin and membranes shapes cell division. Open Biology. 2020;10(3):190314. doi: doi:10.1098/rsob.190314.
3. Burute M, Kapitein LC. Cellular Logistics: Unraveling the Interplay Between Microtubule Organization and Intracellular Transport. Annual Review of Cell and Developmental Biology. 2019;35(1):29-54. doi: 10.1146/annurev-cellbio-100818-125149. PubMed PMID: 31394046.
4. Garcin C, Straube A. Microtubules in cell migration. Essays in Biochemistry. 2019;63(5):509-20. doi: 10.1042/ebc20190016.
5. McNally FJ. Mechanisms of spindle positioning. The Journal of cell biology. 2013;200(2):131-40.
6. Forth S, Kapoor TM. The mechanics of microtubule networks in cell division. J Cell Biol. 2017;216(6):1525-31.
7. Kotak S. Mechanisms of Spindle Positioning: Lessons from Worms and Mammalian Cells. Biomolecules. 2019;9(2):80. PubMed PMID: doi:10.3390/biom9020080.
8. Thomas GE, Renjith MR, Manna TK. Kinetochore–microtubule interactions in chromosome segregation: lessons from yeast and mammalian cells. Biochemical Journal. 2017;474(21):3559-77. doi: 10.1042/bcj20170518.
9. Lechler T, Mapelli M. Spindle positioning and its impact on vertebrate tissue architecture and cell fate. Nature Reviews Molecular Cell Biology. 2021;22(10):691-708. doi: 10.1038/s41580-021-00384-4.
10. di Pietro F, Echard A, Morin X. Regulation of mitotic spindle orientation: an integrated view. EMBO reports. 2016. doi: 10.15252/embr.201642292.
11. van Leen EV, di Pietro F, Bellaïche Y. Oriented cell divisions in epithelia: from force generation to force anisotropy by tension, shape and vertices. Current Opinion in Cell Biology. 2020;62:9-16. doi: https://doi.org/10.1016/j.ceb.2019.07.013.
12. Goodson HV, Jonasson EM. Microtubules and microtubule-associated proteins. Cold Spring Harbor perspectives in biology. 2018;10(6):a022608.
13. Akhmanova A, Kapitein LC. Mechanisms of microtubule organization in differentiated animal cells. Nature Reviews Molecular Cell Biology. 2022;23(8):541-58. doi: 10.1038/s41580-022-00473-y.
14. Gudimchuk NB, McIntosh JR. Regulation of microtubule dynamics, mechanics and function through the growing tip. Nature Reviews Molecular Cell Biology. 2021;22(12):777-95. doi: 10.1038/s41580-021-00399-x.
15. Gittes F, Mickey B, Nettleton J, Howard J. Flexural rigidity of microtubules and actin filaments measured from thermal fluctuations in shape. The Journal of cell biology. 1993;120(4):923-34.
16. Mickey B, Howard J. Rigidity of microtubules is increased by stabilizing agents. The Journal of cell biology. 1995;130(4):909-17.
17. Felgner H, Frank R, Schliwa M. Flexural rigidity of microtubules measured with the use of optical tweezers. Journal of Cell Science. 1996;109(2):509-16.

18. Kurachi M, Hoshi M, Tashiro H. Buckling of a single microtubule by optical trapping forces: direct measurement of microtubule rigidity. Cell motility and the cytoskeleton. 1995;30(3):221-8.
19. Brangwynne CP, MacKintosh FC, Kumar S, Geisse NA, Talbot J, Mahadevan L, et al. Microtubules can bear enhanced compressive loads in living cells because of lateral reinforcement. The Journal of cell biology. 2006;173(5):733-41.
20. Zhang Z, Nishimura Y, Kanchanawong P. Extracting microtubule networks from superresolution single-molecule localization microscopy data. Molecular biology of the cell. 2017;28(2):333-45.
21. Hawkins T, Mirigian M, Yasar MS, Ross JL. Mechanics of microtubules. Journal of biomechanics. 2010;43(1):23-30.
22. Balabanian L, Berger CL, Hendricks AG. Acetylated Microtubules Are Preferentially Bundled Leading to Enhanced Kinesin-1 Motility. Biophysical journal. 2017;113(7):1551-60. doi: 10.1016/j.bpj.2017.08.009.
23. Daga RR, Yonetani A, Chang F. Asymmetric Microtubule Pushing Forces in Nuclear Centering. Current Biology. 2006;16(15):1544-50. doi: 10.1016/j.cub.2006.06.026.
24. Tran P, Marsh L, Doye V, Inoue S, Chang F. A mechanism for nuclear positioning in fission yeast based on microtubule pushing. The Journal of cell biology. 2001;153(2):397-412.
25. Pécréaux J, Redemann S, Alayan Z, Mercat B, Pastezeur S, Garzon-Coral C, et al. The Mitotic Spindle in the One-Cell C. elegans Embryo Is Positioned with High Precision and Stability. Biophysical journal. 2016;111(8):1773-84. doi: https://doi.org/10.1016/j.bpj.2016.09.007.
26. Meaders JL, de Matos SN, Burgess DR. A Pushing Mechanism for Microtubule Aster Positioning in a Large Cell Type. Cell Reports. 2020;33(1):108213. doi: https://doi.org/10.1016/j.celrep.2020.108213.
27. Garzon-Coral C, Fantana HA, Howard J. A force-generating machinery maintains the spindle at the cell center during mitosis. Science. 2016;352(6289):1124-7. doi: 10.1126/science.aad9745.
28. Tolic-Nørrelykke IM, Sacconi L, Thon G, Pavone FS. Positioning and elongation of the fission yeast spindle by microtubule-based pushing. Current biology. 2004;14(13):1181-6.
29. Schneider MWG, Gibson BA, Otsuka S, Spicer MFD, Petrovic M, Blaukopf C, et al. A mitotic chromatin phase transition prevents perforation by microtubules. Nature. 2022. doi: 10.1038/s41586-022-05027-y.
30. Maiato H, Gomes AM, Sousa F, Barisic M. Mechanisms of Chromosome Congression during Mitosis. Biology. 2017;6(1):13. PubMed PMID: doi:10.3390/biology6010013.
31. Arjona MI, Najafi J, Minc N. Cytoplasm mechanics and cellular organization. Current Opinion in Cell Biology. 2023;85:102278. doi: https://doi.org/10.1016/j.ceb.2023.102278.
32. Felgner H, Frank R, Biernat J, Mandelkow E-M, Mandelkow E, Ludin B, et al. Domains of neuronal microtubule-associated proteins and flexural rigidity of microtubules. The Journal of cell biology. 1997;138(5):1067-75.
33. Nishida K, Matsumura K, Tamura M, Nakamichi T, Shimamori K, Kuragano M, et al. Effects of three microtubule-associated proteins (MAP2, MAP4, and Tau) on microtubules' physical properties and neurite morphology. Scientific Reports. 2023;13(1):8870. doi: 10.1038/s41598-023-36073-9.
34. Jean DC, Baas PW, Black MM. A novel role for doublecortin and doublecortin-like kinase in regulating growth cone microtubules. Human molecular genetics. 2012;21(26):5511-27. Epub 2012/09/21. doi: 10.1093/hmg/dds395. PubMed PMID: 23001563.

35. Moores CA, Perderiset M, Francis F, Chelly J, Houdusse A, Milligan RA. Mechanism of microtubule stabilization by doublecortin. Molecular cell. 2004;14(6):833-9.
36. Fourniol FJ, Sindelar CV, Amigues B, Clare DK, Thomas G, Perderiset M, et al. Template-free 13-protofilament microtubule–MAP assembly visualized at 8 Å resolution. The Journal of Cell Biology. 2010;191(3):463-70. doi: 10.1083/jcb.201007081.
37. Pampaloni F, Lattanzi G, Jonáš A, Surrey T, Frey E, Florin E-L. Thermal fluctuations of grafted microtubules provide evidence of a length-dependent persistence length. Proceedings of the National Academy of Sciences. 2006;103(27):10248-53.
38. Sui H, Downing KH. Structural basis of interprotofilament interaction and lateral deformation of microtubules. Structure. 2010;18(8):1022-31.
39. Hahn I, Voelzmann A, Parkin J, Fülle JB, Slater PG, Lowery LA, et al. Tau, XMAP215/Msps and Eb1 co-operate interdependently to regulate microtubule polymerisation and bundle formation in axons. PLOS Genetics. 2021;17(7):e1009647. doi: 10.1371/journal.pgen.1009647.
40. Kadavath H, Hofele RV, Biernat J, Kumar S, Tepper K, Urlaub H, et al. Tau stabilizes microtubules by binding at the interface between tubulin heterodimers. Proceedings of the National Academy of Sciences. 2015;112(24):7501-6. doi: doi:10.1073/pnas.1504081112.
41. Kellogg EH, Hejab NMA, Poepsel S, Downing KH, DiMaio F, Nogales E. Near-atomic model of microtubule-tau interactions. Science. 2018;360(6394):1242-6. doi: 10.1126/science.aat1780.
42. Srayko M, Kaya A, Stamford J, Hyman AA. Identification and Characterization of Factors Required for Microtubule Growth and Nucleation in the Early C. elegans Embryo. Developmental Cell. 2005;9(2):223-36.
43. Dema A, Charafeddine RA, van Haren J, Rahgozar S, Viola G, Jacobs KA, et al. Doublecortin reinforces microtubules to promote growth cone advance in soft environments. Current Biology. 2024. doi: https://doi.org/10.1016/j.cub.2024.10.063.
44. Bunker JM, Wilson L, Jordan MA, Feinstein SC. Modulation of microtubule dynamics by tau in living cells: implications for development and neurodegeneration. Molecular biology of the cell. 2004;15(6):2720-8.
45. Shu T, Tseng H-C, Sapir T, Stern P, Zhou Y, Sanada K, et al. Doublecortin-like kinase controls neurogenesis by regulating mitotic spindles and M phase progression. Neuron. 2006;49(1):25-39.
46. Vreugdenhil E, Kolk SM, Boekhoorn K, Fitzsimons CP, Schaaf M, Schouten T, et al. Doublecortin-like, a microtubule-associated protein expressed in radial glia, is crucial for neuronal precursor division and radial process stability. European Journal of Neuroscience. 2007;25(3):635-48. doi: https://doi.org/10.1111/j.1460-9568.2007.05318.x.
47. Kaplan A, Reiner O. Linking cytoplasmic dynein and transport of Rab8 vesicles to the midbody during cytokinesis by the doublecortin domain-containing 5 protein. Journal of cell science. 2011;124(23):3989-4000.
48. Gönczy P, Bellanger JM, Kirkham M, Pozniakowski A, Baumer K, Phillips JB, et al. zyg-8, a gene required for spindle positioning in C. elegans, encodes a doublecortin-related kinase that promotes microtubule assembly. Developmental cell. 2001;1(3):363.
49. Li W, Crellin HA, Cheerambathur D, McNally FJ. Redundant microtubule crosslinkers prevent meiotic spindle bending to ensure diploid offspring in C. elegans. PLOS Genetics. 2023;19(12):e1011090. doi: 10.1371/journal.pgen.1011090.

50. Czajkowski ER, Zou Y, Divekar NS, Wignall SM. The doublecortin-family kinase ZYG-8DCLK1 regulates microtubule dynamics and motor-driven forces to promote the stability of C. elegans acentrosomal spindles. PLoS genetics. 2024;20(9):e1011373.
51. Couillard-Despres S, Uyanik G, Ploetz S, Karl C, Koch H, Winkler J, et al. Mitotic impairment by doublecortin is diminished by doublecortin mutations found in patients. Neurogenetics. 2004;5(2):83-93. doi: 10.1007/s10048-004-0176-1.
52. Rossi G, Dalprà L, Crosti F, Lissoni S, Sciacca FL, Catania M, et al. A new function of microtubule-associated protein tau: involvement in chromosome stability. Cell Cycle. 2008;7(12):1788-94. Epub 2008/06/28. doi: 10.4161/cc.7.12.6012. PubMed PMID: 18583940.
53. Bougé A-L, Parmentier M-L. Tau excess impairs mitosis and kinesin-5 function, leading to aneuploidy and cell death. Disease Models & Mechanisms. 2016;9(3):307-19. doi: 10.1242/dmm.022558.
54. Liu JS, Schubert CR, Fu X, Fourniol FJ, Jaiswal JK, Houdusse A, et al. Molecular basis for specific regulation of neuronal kinesin-3 motors by doublecortin family proteins. Molecular cell. 2012;47(5):707-21.
55. Rose L, Gönczy P. Polarity establishment, asymmetric division and segregation of fate determinants in early C. elegans embryos. WormBook: the online review of C elegans biology. 2013:1-43.
56. Oegema K, Hyman T. Cell division. WormBook: The Online Review of C elegans Biology. 2006.
57. Pécréaux J, Röper J-C, Kruse K, Jülicher F, Hyman AA, Grill SW, et al. Spindle Oscillations during Asymmetric Cell Division Require a Threshold Number of Active Cortical Force Generators. Curr Biol. 2006;16(21):2111-22. doi: 10.1016/j.cub.2006.09.030.
58. Kozlowski C, Srayko M, Nedelec F. Cortical Microtubule Contacts Position the Spindle in C. elegans Embryos. Cell. 2007;129(3):499-510. doi: https://doi.org/10.1016/j.cell.2007.03.027.
59. Wu H-Y, Kabacaoğlu G, Nazockdast E, Chang H-C, Shelley MJ, Needleman DJ. Laser ablation and fluid flows reveal the mechanism behind spindle and centrosome positioning. Nature Physics. 2023. doi: 10.1038/s41567-023-02223-z.
60. Grill SW, Kruse K, Jülicher F. Theory of Mitotic Spindle Oscillations. Physical Review Letters. 2005;94(10):108104.
61. Valfort A-C, Launay C, Sémon M, Delattre M. Evolution of mitotic spindle behavior during the first asymmetric embryonic division of nematodes. PLoS Biology. 2018;16(1):e2005099. doi: 10.1371/journal.pbio.2005099. PubMed PMID: PMC5794175.
62. Riche S, Zouak M, Argoul F, Arneodo A, Pecreaux J, Delattre M. Evolutionary comparisons reveal a positional switch for spindle pole oscillations in Caenorhabditis embryos. The Journal of cell biology. 2013;201(5):653-62.
63. Bouvrais H, Chesneau L, Pastezeur S, Fairbrass D, Delattre M, Pécréaux J. Microtubule Feedback and LET-99-Dependent Control of Pulling Forces Ensure Robust Spindle Position. Biophysical journal. 2018;115(11):2189-205. doi: https://doi.org/10.1016/j.bpj.2018.10.010.
64. Howard J, Garzon-Coral C. Physical Limits on the Precision of Mitotic Spindle Positioning by Microtubule Pushing forces. BioEssays. 2017;39(11):1700122. doi: doi:10.1002/bies.201700122.
65. Nguyen-Ngoc T, Afshar K, Gonczy P. Coupling of cortical dynein and G[alpha] proteins mediates spindle positioning in Caenorhabditis elegans. Nat Cell Biol. 2007;9(11):1294-302. doi: http://www.nature.com/ncb/journal/v9/n11/suppinfo/ncb1649_S1.html.

66. Grill SW, Hyman AA. Spindle positioning by cortical pulling forces. Developmental Cell. 2005;8(4):461-5.
67. Kimura K, Kimura A. Intracellular organelles mediate cytoplasmic pulling force for centrosome centration in the Caenorhabditis elegans early embryo. Proceedings of the National Academy of Sciences. 2011;108(1):137-42.
68. Howard J. Elastic and damping forces generated by confined arrays of dynamic microtubules. Physical biology. 2006;3:54.
69. Grill SW, Howard J, Schaffer E, Stelzer EHK, Hyman AA. The distribution of active force generators controls mitotic spindle position. Science. 2003;301(5632):518.
70. Farhadifar R, Yu C-H, Fabig G, Wu H-Y, Stein DB, Rockman M, et al. Stoichiometric interactions explain spindle dynamics and scaling across 100 million years of nematode evolution. Elife. 2020;9:e55877. doi: 10.7554/eLife.55877.
71. Bouvrais H, Chesneau L, Le Cunff Y, Fairbrass D, Soler N, Pastezeur S, et al. The coordination of spindle-positioning forces during the asymmetric division of the Caenorhabditis elegans zygote. EMBO reports. 2021;22(5):e50770. doi: https://doi.org/10.15252/embr.202050770.
72. Bellanger J-M, Carter JC, Phillips JB, Canard C, Bowerman B, Gönczy P. ZYG-9, TAC-1 and ZYG-8 together ensure correct microtubule function throughout the cell cycle of C. elegans embryos. Journal of Cell Science. 2007;120(16):2963-73.
73. Agulto RL, Rogers MM, Tan TC, Ramkumar A, Downing AM, Bodin H, et al. Autoregulatory control of microtubule binding in doublecortin-like kinase 1. Elife. 2021;10:e60126. doi: 10.7554/eLife.60126.
74. Wood WB, Hecht R, Carr S, Vanderslice R, Wolf N, Hirsh D. Parental effects and phenotypic characterization of mutations that affect early development in Caenorhabditis elegans. Developmental Biology. 1980;74(2):446-69. doi: https://doi.org/10.1016/0012-1606(80)90445-5.
75. Srayko M, Quintin S, Schwager A, Hyman AA. Caenorhabditis elegans TAC-1 and ZYG-9 form a complex that is essential for long astral and spindle microtubules. Current biology: CB. 2003;13(17):1506.
76. Brouhard GJ, Stear JH, Noetzel TL, Al-Bassam J, Kinoshita K, Harrison SC, et al. XMAP215 Is a Processive Microtubule Polymerase. Cell. 2008;132(1):79-88. doi: 10.1016/j.cell.2007.11.043.
77. Piehl M, Tulu US, Wadsworth P, Cassimeris L. Centrosome maturation: measurement of microtubule nucleation throughout the cell cycle by using GFP-tagged EB1. Proceedings of the National Academy of Sciences. 2004;101(6):1584-8.
78. Decker M, Jaensch S, Pozniakovsky A, Zinke A, O'Connell Kevin F, Zachariae W, et al. Limiting Amounts of Centrosome Material Set Centrosome Size in C. elegans Embryos. Current Biology. 2011;21(15):1259-67. doi: 10.1016/j.cub.2011.06.002.
79. Baumgart J, Kirchner M, Redemann S, Bond A, Woodruff J, Verbavatz J-M, et al. Soluble tubulin is significantly enriched at mitotic centrosomes. Journal of Cell Biology. 2019;218(12):3977-85.
80. Woodruff JB, Wueseke O, Viscardi V, Mahamid J, Ochoa SD, Bunkenborg J, et al. Regulated assembly of a supramolecular centrosome scaffold in vitro. Science. 2015;348(6236):808-12. doi: doi:10.1126/science.aaa3923.
81. Horesh D, Sapir T, Francis F, Wolf SG, Caspi M, Elbaum M, et al. Doublecortin, a stabilizer of microtubules. Human molecular genetics. 1999;8(9):1599-610.

82. Moores CA, Perderiset M, Kappeler C, Kain S, Drummond D, Perkins SJ, et al. Distinct roles of doublecortin modulating the microtubule cytoskeleton. The EMBO Journal. 2006;25(19):4448-57. doi: https://doi.org/10.1038/sj.emboj.7601335.
83. Manka SW, Moores CA. Pseudo-repeats in doublecortin make distinct mechanistic contributions to microtubule regulation. EMBO reports. 2020;21(12):e51534. doi: https://doi.org/10.15252/embr.202051534.
84. Espiritu EB, Krueger LE, Ye A, Rose LS. CLASPs function redundantly to regulate astral microtubules in the C. elegans embryo. Developmental biology. 2012;368(2):242-54. Epub 2012/05/23. doi: 10.1016/j.ydbio.2012.05.016. PubMed PMID: 22613359; PubMed Central PMCID: PMCPMC3600381.
85. Lacroix B, Letort G, Pitayu L, Sallé J, Stefanutti M, Maton G, et al. Microtubule Dynamics Scale with Cell Size to Set Spindle Length and Assembly Timing. Developmental Cell. 2018;45(4):496-511.e6. doi: https://doi.org/10.1016/j.devcel.2018.04.022.
86. Al-Bassam J, Kim H, Brouhard G, van Oijen A, Harrison SC, Chang F. CLASP promotes microtubule rescue by recruiting tubulin dimers to the microtubule. Developmental Cell. 2010;19(2):245-58.
87. Walczak CE, Gayek S, Ohi R. Microtubule-Depolymerizing Kinesins. Annual Review of Cell and Developmental Biology. 2013;29(1):417-41. doi: 10.1146/annurev-cellbio-101512-122345. PubMed PMID: 23875646.
88. Cheeseman IM, MacLeod I, Yates JR, Oegema K, Desai A. The CENP-F-like Proteins HCP-1 and HCP-2 Target CLASP to Kinetochores to Mediate Chromosome Segregation. Current Biology. 2005;15(8):771-7. doi: https://doi.org/10.1016/j.cub.2005.03.018.
89. Edwards F, Maton G, Gareil N, Canman JC, Dumont J. BUB-1 promotes amphitelic chromosome biorientation via multiple activities at the kinetochore. Elife. 2018;7:e40690. doi: 10.7554/eLife.40690.
90. Grill SW, Gönczy P, Stelzer EHK, Hyman AA. Polarity controls forces governing asymmetric spindle positioning in the Caenorhabditis elegans embryo. Nature. 2001;409:630-3.
91. Grill SW, GoÈnczy P, Stelzer EHK, Hyman AA. Polarity controls forces governing asymmetric spindle positioning in theCaenorhabditis elegansembryo. 2001.
92. Bellanger J-M, Cueva JG, Baran R, Tang G, Goodman MB, Debant A. The doublecortin-related gene zyg-8 is a microtubule organizer in Caenorhabditis elegans neurons. Journal of Cell Science. 2012;125(22):5417-27.
93. Kikumoto M, Kurachi M, Tosa V, Tashiro H. Flexural rigidity of individual microtubules measured by a buckling force with optical traps. Biophysical journal. 2006;90(5):1687-96.
94. Kurz JC, Williams Jr RC. Microtubule-associated proteins and the flexibility of microtubules. Biochemistry. 1995;34(41):13374-80.
95. Venier P, Maggs AC, Carlier M-F, Pantaloni D. Analysis of microtubule rigidity using hydrodynamic flow and thermal fluctuations. Journal of biological chemistry. 1994;269(18):13353-60.
96. Bicek AD, Tüzel E, Demtchouk A, Uppalapati M, Hancock WO, Kroll DM, et al. Anterograde Microtubule Transport Drives Microtubule Bending in LLC-PK1 Epithelial Cells. Molecular biology of the cell. 2009;20(12):2943-53. doi: 10.1091/mbc.e08-09-0909. PubMed PMID: 19403700.
97. Blob A, Ventzke D, Rölleke U, Nies G, Munk A, Schaedel L, et al. Global alignment and local curvature of microtubules in mouse fibroblasts are robust against perturbations of vimentin and actin. Soft matter. 2025. doi: 10.1039/D4SM01127A.

98. Tsitkov S, Rodriguez JB, Bassir Kazeruni NM, Sweet M, Nitta T, Hess H. The rate of microtubule breaking increases exponentially with curvature. Scientific Reports. 2022;12(1):20899. doi: 10.1038/s41598-022-24912-0.
99. Odde DJ, Ma L, Briggs AH, DeMarco A, Kirschner MW. Microtubule bending and breaking in living fibroblast cells. Journal of Cell Science. 1999;112(19):3283-8. doi: 10.1242/jcs.112.19.3283.
100. Janson ME, Mathilde E, Dogterom M. Dynamic instability of microtubules is regulated by force. The Journal of cell biology. 2003;161(6):1029-34.
101. Komarova YA, Vorobjev IA, Borisy GG. Life cycle of MTs: persistent growth in the cell interior, asymmetric transition frequencies and effects of the cell boundary. Journal of Cell Science. 2002;115(17):3527-39.
102. Nedelec F, Foethke D. Collective Langevin dynamics of flexible cytoskeletal fibers. New Journal of Physics. 2007;9(11):427.
103. McDermott JB, Aamodt S, Aamodt E. ptl-1, a Caenorhabditis elegans gene whose products are homologous to the τ microtubule-associated proteins. Biochemistry. 1996;35(29):9415-23.
104. Goedert M, Baur C, Ahringer J, Jakes R, Hasegawa M, Spillantini M, et al. PTL-1, a microtubule-associated protein with tau-like repeats from the nematode Caenorhabditis elegans. Journal of cell science. 1996;109(11):2661-72.
105. Tintori Sophia C, Osborne Nishimura E, Golden P, Lieb Jason D, Goldstein B. A Transcriptional Lineage of the Early C. elegans Embryo. Developmental Cell. 2016;38(4):430-44. doi: https://doi.org/10.1016/j.devcel.2016.07.025.
106. Glotzer M. The 3Ms of central spindle assembly: microtubules, motors and MAPs. Nature Reviews Molecular Cell Biology. 2009;10(1):9-20. doi: 10.1038/nrm2609.
107. Maurer SP, Fourniol FJ, Bohner G, Moores CA, Surrey T. EBs recognize a nucleotide-dependent structural cap at growing microtubule ends. Cell. 2012;149(2):371-82.
108. Manka Szymon W, Moores Carolyn A. Microtubule structure by cryo-EM: snapshots of dynamic instability. Essays In Biochemistry. 2018. doi: 10.1042/ebc20180031.
109. Bechstedt S, Brouhard GJ. Doublecortin recognizes the 13-protofilament microtubule cooperatively and tracks microtubule ends. Developmental Cell. 2012;23(1):181-92.
110. Ettinger A, van Haren J, Ribeiro Susana A, Wittmann T. Doublecortin Is Excluded from Growing Microtubule Ends and Recognizes the GDP-Microtubule Lattice. Current Biology. 2016;26(12):1549-55. doi: https://doi.org/10.1016/j.cub.2016.04.020.
111. Tsuchiya K, Goshima G. Microtubule-associated proteins promote microtubule generation in the absence of γ-tubulin in human colon cancer cells. Journal of Cell Biology. 2021;220(12). doi: 10.1083/jcb.202104114.
112. Rogers G, Rusan N, Peifer M, Rogers S. A Multicomponent Assembly Pathway Contributes to the Formation of Acentrosomal Microtubule Arrays in Interphase Drosophila Cells. Molecular biology of the cell. 2008;19:3163-78. doi: 10.1091/mbc.E07-10-1069.
113. Lin PT, Gleeson JG, Corbo JC, Flanagan L, Walsh CA. DCAMKL1 Encodes a Protein Kinase with Homology to Doublecortin that Regulates Microtubule Polymerization. The Journal of Neuroscience. 2000;20(24):9152-61. doi: 10.1523/jneurosci.20-24-09152.2000.
114. Tint I, Jean D, Baas PW, Black MM. Doublecortin associates with microtubules preferentially in regions of the axon displaying actin-rich protrusive structures. Journal of Neuroscience. 2009;29(35):10995-1010.

115. Kim MH, Cierpicki T, Derewenda U, Krowarsch D, Feng Y, Devedjiev Y, et al. The DCX-domain tandems of doublecortin and doublecortin-like kinase. Nature Structural & Molecular Biology. 2003;10(5):324-33. doi: 10.1038/nsb918.
116. Bielas SL, Serneo FF, Chechlacz M, Deerinck TJ, Perkins GA, Allen Patrick B, et al. Spinophilin Facilitates Dephosphorylation of Doublecortin by PP1 to Mediate Microtubule Bundling at the Axonal Wrist. Cell. 2007;129(3):579-91. doi: 10.1016/j.cell.2007.03.023.
117. Redemann S, Baumgart J, Lindow N, Shelley M, Nazockdast E, Kratz A, et al. C. elegans chromosomes connect to centrosomes by anchoring into the spindle network. Nature Communications. 2017;8:15288. doi: 10.1038/ncomms15288
https://www.nature.com/articles/ncomms15288#supplementary-information.
118. Portran D, Schaedel L, Xu Z, Théry M, Nachury Maxence V. Tubulin acetylation protects long-lived microtubules against mechanical ageing. Nature Cell Biology. 2017;19:391. doi: 10.1038/ncb3481
https://www.nature.com/articles/ncb3481#supplementary-information.
119. Wall KP, Hart H, Lee T, Page C, Hawkins TL, Hough LE. C-Terminal Tail Polyglycylation and Polyglutamylation Alter Microtubule Mechanical Properties. Biophysical journal. 2020;119(11):2219-30. doi: https://doi.org/10.1016/j.bpj.2020.09.040.
120. Xu Z, Schaedel L, Portran D, Aguilar A, Gaillard J, Marinkovich MP, et al. Microtubules acquire resistance from mechanical breakage through intralumenal acetylation. Science. 2017;356(6335):328-32. doi: 10.1126/science.aai8764.
121. Nishi K, Raja S, Pham A, Freeman R, Roll-Mecak A, MacKintosh FC, et al. Nonequilibrium bending fluctuations reveal microtubule mechanics in-vivo and their regulation by glutamylation. bioRxiv. 2023:2023.10.26.564252. doi: 10.1101/2023.10.26.564252.
122. Robison P, Caporizzo MA, Ahmadzadeh H, Bogush AI, Chen CY, Margulies KB, et al. Detyrosinated microtubules buckle and bear load in contracting cardiomyocytes. Science. 2016;352(6284):aaf0659. doi: doi:10.1126/science.aaf0659.
123. Sébastien M, Paquette AL, Prowse ENP, Hendricks AG, Brouhard GJ. Doublecortin restricts neuronal branching by regulating tubulin polyglutamylation. Nature Communications. 2025;16(1):1749. doi: 10.1038/s41467-025-56951-2.
124. Chawla DG, Shah RV, Barth ZK, Lee JD, Badecker KE, Naik A, et al. Caenorhabditis elegans glutamylating enzymes function redundantly in male mating. Biology Open. 2016;5(9):1290-8. doi: 10.1242/bio.017442.
125. Schaedel L, John K, Gaillard J, Nachury MV, Blanchoin L, Théry M. Microtubules self-repair in response to mechanical stress. Nature Materials. 2015;14(11):1156-63. doi: 10.1038/nmat4396.
126. Aher A, Rai D, Schaedel L, Gaillard J, John K, Liu Q, et al. CLASP Mediates Microtubule Repair by Restricting Lattice Damage and Regulating Tubulin Incorporation. Current Biology. 2020;30(11):2175-83.e6. doi: https://doi.org/10.1016/j.cub.2020.03.070.
127. Théry M, Blanchoin L. Microtubule self-repair. Current Opinion in Cell Biology. 2021;68:144-54. doi: https://doi.org/10.1016/j.ceb.2020.10.012.
128. Chrétien D, Metoz F, Verde F, Karsenti E, Wade RH. Lattice defects in microtubules: protofilament numbers vary within individual microtubules. The Journal of cell biology. 1992;117(5):1031-40.
129. Schaedel L, Triclin S, Chrétien D, Abrieu A, Aumeier C, Gaillard J, et al. Lattice defects induce microtubule self-renewal. Nature Physics. 2019. doi: 10.1038/s41567-019-0542-4.

130. Chaaban S, Jariwala S, Hsu C-T, Redemann S, Kollman JM, Müller-Reichert T, et al. The Structure and Dynamics of C. elegans Tubulin Reveals the Mechanistic Basis of Microtubule Growth. Developmental Cell. 2018. doi: https://doi.org/10.1016/j.devcel.2018.08.023.
131. Wu JC, Rose LS. PAR-3 and PAR-1 inhibit LET-99 localization to generate a cortical band important for spindle positioning in Caenorhabditis elegans embryos. Molecular biology of the cell. 2007;18(11):4470-82.
132. Redemann S, Pecreaux J, Goehring NW, Khairy K, Stelzer EHK, Hyman AA, et al. Membrane invaginations reveal cortical sites that pull on mitotic spindles in one-cell C. elegans embryos. PloS one. 2010;5(8):e12301.
133. Fielmich L-E, Schmidt R, Dickinson DJ, Goldstein B, Akhmanova A, Van den Heuvel S. Optogenetic dissection of mitotic spindle positioning in vivo. Elife. 2018;7:e38198. doi: 10.7554/eLife.38198.
134. Dogterom M, Kerssemakers JWJ, Romet-Lemonne G, Janson ME. Force generation by dynamic microtubules. Current Opinion in Cell Biology. 2005;17(1):67-74. doi: https://doi.org/10.1016/j.ceb.2004.12.011.
135. Bergstralh DT, Dawney NS, St Johnston D. Spindle orientation: a question of complex positioning. Development. 2017;144(7):1137-45. doi: 10.1242/dev.140764.
136. Yeltokov A, Finegan TM, Fletcher AG, Lovegrove HE, Bergstralh DT. Beyond pulling: microtubule pushing forces contribute to robust spindle orientation in regular and irregular cell shapes. bioRxiv. 2025:2025.09.22.677921. doi: 10.1101/2025.09.22.677921.
137. Jingchen L, Longcan C, Hongyuan J. Cell shape and intercellular adhesion regulate mitotic spindle orientation. Molecular biology of the cell. 2019;30(19):2458-68. doi: 10.1091/mbc.E19-04-0227. PubMed PMID: 31411941.
138. Mao Y, Tournier AL, Bates PA, Gale JE, Tapon N, Thompson BJ. Planar polarization of the atypical myosin Dachs orients cell divisions in Drosophila. Genes Dev. 2011;25(2):131-6. Epub 2011/01/20. doi: 10.1101/gad.610511. PubMed PMID: 21245166; PubMed Central PMCID: PMCPMC3022259.
139. Strauss B, Adams RJ, Papalopulu N. A default mechanism of spindle orientation based on cell shape is sufficient to generate cell fate diversity in polarised Xenopus blastomeres. Development. 2006;133:3883-93.
140. Tsou MFB, Hayashi A, DeBella LR, McGrath G, Rose LS. LET-99 determines spindle position and is asymmetrically enriched in response to PAR polarity cues in C. elegans embryos. Development. 2002;129(19):4469-81.
141. Singh D, Schmidt N, Müller F, Bange T, Bird AW. Destabilization of Long Astral Microtubules via Cdk1-Dependent Removal of GTSE1 from Their Plus Ends Facilitates Prometaphase Spindle Orientation. Current Biology. 2021;31(4):766-81.e8. doi: 10.1016/j.cub.2020.11.040.
142. Saleh J, Fardin M-A, Barai A, Soleilhac M, Frenoy O, Gaston C, et al. Length limitation of astral microtubules orients cell divisions in murine intestinal crypts. Developmental Cell. 2023;58(17):1519-33.e6. doi: 10.1016/j.devcel.2023.06.004.
143. Izumi Y, Ohta N, Hisata K, Raabe T, Matsuzaki F. Drosophila Pins-binding protein Mud regulates spindle-polarity coupling and centrosome organization. Nature cell biology. 2006;8(6):586-93.
144. Siller KH, Cabernard C, Doe CQ. The NuMA-related Mud protein binds Pins and regulates spindle orientation in Drosophila neuroblasts. Nature Cell Biology. 2006;8(6):594-600.

145. Williams SE, Beronja S, Pasolli HA, Fuchs E. Asymmetric cell divisions promote Notch-dependent epidermal differentiation. Nature. 2011;470(7334):353-8.
146. Fischer E, Legue E, Doyen A, Nato F, Nicolas J-F, Torres V, et al. Defective planar cell polarity in polycystic kidney disease. Nature Genetics. 2006;38(1):21-3. doi: 10.1038/ng1701.
147. Fleming ES, Temchin M, Wu Q, Maggio-Price L, Tirnauer JS. Spindle misorientation in tumors from APC mice. Molecular Carcinogenesis. 2009;48(7):592-8. doi: https://doi.org/10.1002/mc.20506.
148. Pease JC, Tirnauer JS. Mitotic spindle misorientation in cancer – out of alignment and into the fire. Journal of Cell Science. 2011;124(7):1007-16. doi: 10.1242/jcs.081406.
149. Quesada-Hernández E, Caneparo L, Schneider S, Winkler S, Liebling M, Fraser SE, et al. Stereotypical Cell Division Orientation Controls Neural Rod Midline Formation in Zebrafish. Current Biology. 2010;20(21):1966-72. doi: https://doi.org/10.1016/j.cub.2010.10.009.
150. Baena-López LA, Baonza A, García-Bellido A. The Orientation of Cell Divisions Determines the Shape of Drosophila Organs. Current Biology. 2005;15(18):1640-4. doi: https://doi.org/10.1016/j.cub.2005.07.062.
151. Quyn AJ, Appleton PL, Carey FA, Steele RJC, Barker N, Clevers H, et al. Spindle Orientation Bias in Gut Epithelial Stem Cell Compartments Is Lost in Precancerous Tissue. Cell Stem Cell. 2010;6(2):175-81. doi: https://doi.org/10.1016/j.stem.2009.12.007.
152. Gao L, Yang Z, Hiremath C, Zimmerman SE, Long B, Brakeman PR, et al. Afadin orients cell division to position the tubule lumen in developing renal tubules. Development. 2017;144(19):3511-20. Epub 2017/09/02. doi: 10.1242/dev.148908. PubMed PMID: 28860115; PubMed Central PMCID: PMCPMC5665479.
153. Fededa JP, Esk C, Mierzwa B, Stanyte R, Yuan S, Zheng H, et al. MicroRNA-34/449 controls mitotic spindle orientation during mammalian cortex development. The EMBO Journal. 2016;35(22):2386-98. doi: https://doi.org/10.15252/embj.201694056.
154. Gao T, Wang M, Xu L, Wen T, Liu J, An G. DCLK1 is up-regulated and associated with metastasis and prognosis in colorectal cancer. J Cancer Res Clin Oncol. 2016;142(10):2131-40. Epub 2016/08/16. doi: 10.1007/s00432-016-2218-0. PubMed PMID: 27520310.
155. Ge Y, Weygant N, Qu D, May R, Berry WL, Yao J, et al. Alternative splice variants of DCLK1 mark cancer stem cells, promote self-renewal and drug-resistance, and can be targeted to inhibit tumorigenesis in kidney cancer. Int J Cancer. 2018;143(5):1162-75. Epub 2018/03/27. doi: 10.1002/ijc.31400. PubMed PMID: 29577277.
156. Ito H, Tanaka S, Akiyama Y, Shimada S, Adikrisna R, Matsumura S, et al. Dominant expression of DCLK1 in human pancreatic cancer stem cells accelerates tumor invasion and metastasis. PLoS One. 2016;11(1):e0146564.
157. Liu H, Wen T, Zhou Y, Fan X, Du T, Gao T, et al. DCLK1 plays a metastatic-promoting role in human breast cancer cells. BioMed Research International. 2019;2019.
158. Rossi G, Redaelli V, Contiero P, Fabiano S, Tagliabue G, Perego P, et al. Tau mutations serve as a novel risk factor for cancer. Cancer research. 2018;78(13):3731-9.
159. Gargini R, Segura-Collar B, Sánchez-Gómez P. Novel Functions of the Neurodegenerative-Related Gene Tau in Cancer. Frontiers in Aging Neuroscience. 2019;11(231). doi: 10.3389/fnagi.2019.00231.
160. Papin S, Paganetti P. Emerging Evidences for an Implication of the Neurodegeneration-Associated Protein TAU in Cancer. Brain Sciences. 2020;10(11):862. PubMed PMID: doi:10.3390/brainsci10110862.
161. Brenner S. The genetics of Caenorhabditis elegans. Genetics. 1974;77(1):71-94.

162. Kamath RS, Ahringer J. Genome-wide RNAi screening in Caenorhabditis elegans. Methods. 2003;30(4):313-21. doi: https://doi.org/10.1016/S1046-2023(03)00050-1.
163. Duerr JS. Antibody staining in C. elegans using "freeze-cracking". J Vis Exp. 2013;(80). Epub 2013/10/23. doi: 10.3791/50664. PubMed PMID: 24145964; PubMed Central PMCID: PMCPMC3940349.
164. Li S, Besson S, Blackburn C, Carroll M, Ferguson RK, Flynn H, et al. Metadata management for high content screening in OMERO. Methods. 2016;96:27-32. doi: https://doi.org/10.1016/j.ymeth.2015.10.006.
165. Costes SV, Daelemans D, Cho EH, Dobbin Z, Pavlakis G, Lockett S. Automatic and quantitative measurement of protein-protein colocalization in live cells. Biophysical journal. 2004;86(6):3993-4003. Epub 2004/06/11. doi: 10.1529/biophysj.103.038422. PubMed PMID: 15189895; PubMed Central PMCID: PMCPMC1304300.
166. Bolte S, Cordelières FP. A guided tour into subcellular colocalization analysis in light microscopy. Journal of Microscopy. 2006;224(3):213-32. doi: https://doi.org/10.1111/j.1365-2818.2006.01706.x.
167. Schindelin J, Arganda-Carreras I, Frise E, Kaynig V, Longair M, Pietzsch T, et al. Fiji: an open-source platform for biological-image analysis. Nature methods. 2012;9(7):676-82. doi: 10.1038/nmeth.2019.
168. Pécréaux J, Zimmer C, Olivo-Marin J-C, editors. Biophysical active contours for cell tracking I: Tension and bending. Image Processing, 2006 IEEE International Conference on; 2006: IEEE.
169. Kalman RE. A new approach to linear filtering and prediction problems. Journal of basic Engineering. 1960;82(1):35-45.
170. de Chaumont F, Dallongeville S, Chenouard N, Hervé N, Pop S, Provoost T, et al. Icy: an open bioimage informatics platform for extended reproducible research. Nature methods. 2012;9:690. doi: 10.1038/nmeth.2075
https://www.nature.com/articles/nmeth.2075#supplementary-information.
171. Soler N, Da Silva M, Tascon C, Chesneau L, Foliard P, Bouvrais H, et al. Kinesin-12 KLP-18 contributes to the kinetochore-microtubule poleward flux during the metaphase of C. elegans one-cell embryo. bioRxiv. 2025:2022.11.07.515476. doi: 10.1101/2022.11.07.515476.
172. Kolin D. Image correlation spectroscopy. 2003.
173. Jaqaman K, Loerke D, Mettlen M, Kuwata H, Grinstein S, Schmid SL, et al. Robust single-particle tracking in live-cell time-lapse sequences. Nat Methods. 2008;5(8):695-702. Epub 2008/07/22. doi: 10.1038/nmeth.1237. PubMed PMID: 18641657; PubMed Central PMCID: PMC2747604.
174. Forster B, Van De Ville D, Berent J, Sage D, Unser M, editors. Extended depth-of-focus for multi-channel microscopy images: a complex wavelet approach. Biomedical Imaging: Nano to Macro, 2004 IEEE International Symposium on; 2004: IEEE.
175. Sandberg K, Brega M. Segmentation of thin structures in electron micrographs using orientation fields. Journal of Structural Biology. 2007;157(2):403-15. doi: https://doi.org/10.1016/j.jsb.2006.09.007.
176. Bicek AD, Tüzel E, Kroll DM, Odde DJ. Analysis of Microtubule Curvature. Methods in Cell Biology. 83: Academic Press; 2007. p. 237-68.
177. Kroon D-J. 2D line curvature and normals. Mathworks; 2011.

178. Sugioka K, Fielmich L-E, Mizumoto K, Bowerman B, van den Heuvel S, Kimura A, et al. Tumor suppressor APC is an attenuator of spindle-pulling forces during C. elegans asymmetric cell division. Proceedings of the National Academy of Sciences. 2018:201712052.
179. Mercat B. Analyse temps-fréquence en mécanique cellulaire et adaptabilité du fuseau mitotique: Univesité de rennes 1; 2016.
180. harris f. On the Use of Windows for Harmonic Analysis With the Discrete Fourier Transform. Proceedings of the IEEE. 1978;66:51-83. doi: 10.1109/PROC.1978.10837.
181. Pierre DA, Lowe MJ. Mathematical programming via augmented lagrangians: An introduction with computer programs. (No Title). 1975.
182. Audet C, Dennis Jr JE. Analysis of generalized pattern searches. SIAM Journal on optimization. 2002;13(3):889-903.
183. DiCiccio TJ, Efron B. Bootstrap confidence intervals. Statistical science. 1996;11(3):189-228.
184. Efron B, Tibshirani RJ. An introduction to the bootstrap: Chapman and Hall/CRC; 1994.